Cross section measurements of neutron elastic and inelastic scattering on ^{54}Fe

G. Gkatis,[1,2,*] M. Diakaki,[2] G. Noguere,[1] M. Nyman,[3] A. Oprea,[4] C. Paradela,[4] E. Pirovano,[5] and A. J. M. Plompen[4]

[1]*CEA/DES/IRESNE/DER/SPRC/LEPh, Cadarache, F-13108 Saint Paul Lez Durance, France*
[2]*Department of Physics, National Technical University of Athens, GR-15780 Athens, Greece*
[3]*Department of Chemistry, University of Helsinki, FI-00014 Helsinki, Finland*
[4]*Joint Research Centre, European Commission, B-2440 Geel, Belgium*
[5]*Physikalisch-Technische Bundesanstalt, D-38116 Braunschweig, Germany*

(Received 15 December 2023; accepted 16 January 2024; published 15 March 2024)

Scattering experiments were performed at the Geel Electron Linear Accelerator (GELINA) to determine the differential cross sections of neutron elastic and inelastic scattering on ^{54}Fe, using a highly enriched sample. Neutron energies were calculated via the time-of-flight technique. The scattered neutrons were detected using the ELastic and Inelastic Scattering Array (ELISA), a spectrometer consisting of 32 liquid organic scintillators, able to separate neutron and photon induced events via pulse-shape analysis. The detectors are mounted at eight specific angles with respect to the neutron beam direction to allow the concurrent calculation of both the differential and the integral cross section using the Gauss-Legendre quadrature rule. For elastic scattering, angular distributions and integral cross sections were produced in the energy range from 1 to 8 MeV, whereas for inelastic scattering, partial differential and angle integrated cross sections were estimated from the first excited state of ^{54}Fe in the energy range from 2.5 to 5.5 MeV. The results are compared with the available experimental and evaluated nuclear data, as well as with theoretical calculations performed with the TALYS 1.9 and EMPIRE 3.2 codes.

DOI: 10.1103/PhysRevC.109.034612

I. INTRODUCTION

Iron is a major structural material used in a variety of nuclear applications. In nuclear power reactors, iron is used to make pressure vessels and structural supports for the reactor core due to its corrosion resistance, strength, and ability to maintain structural integrity even at high temperatures. During reactor operation the steel alloy components are exposed to a high neutron flux, thus accurate neutron cross section data, that are used in neutron transport models, are indispensable for safe and reliable operation.

Sensitivity and uncertainty studies have shown that uncertainties on the evaluated data of neutron cross sections on iron have a big impact on the most significant integral parameters related to the development of innovative reactor systems [1]. As indicated in [2], neutron elastic scattering on iron nuclides is a major contributor to the uncertainty of the coolant expansion coefficients for the MYRRHA reactor [3]. Specifically, for the ^{54}Fe(n, n) reaction, it is stated that relative uncertainties up to 500% are observed in the JEFF-3.3 [4] evaluation in the MYRRHA relevant energy range (0.1 keV to 4.0 MeV). In an effort to address these uncertainties, iron was included in the Collaborative International Evaluated Library Organization (CIELO) [5] project. It was realized that even though ^{56}Fe amounts for 91.8% of natural iron, validation results are sensitive to the minor iron isotopes ^{54}Fe (5.8%), ^{57}Fe (2.1%), and ^{58}Fe (0.3%) in both the resolved resonance and fast neutron energy region. Furthermore, concerns were expressed about the angular distributions of the elastic and inelastic scattering channels, data that are playing a crucial role in shielding, reflection and leakage. Especially for elastic scattering, the lack of angular distributions below 4 MeV was emphasized, since it was concluded that these data are important in calculating criticality and deep penetration experiments [6]. Scattering cross sections and neutron angular distributions of iron isotopes are also subjects under study by the International Nuclear Data Evaluation Network (INDEN) [7] as a continuation of the CIELO project.

Theoretical calculations in the energy range from 1 to 8 MeV are known to perform poorly in the Cr-Ni region [8]. In the case of the iron isotopes, resonances are causing strong fluctuations on the cross sections in this neutron energy range. On the one hand, the current resolved resonance range evaluation methodology using the *R*-matrix theory is only able to properly reproduce the experimental cross sections up to 700 keV neutron incident energy, and on the other hand statistical model calculations using the Hauser-Feshbach theory are able to reproduce well the continuum cross section only above 6 MeV neutron energy [9]. Since both theoretical approaches are not performing well in the energy range of 1 to

*georgios.gkatis@cea.fr

TABLE I. Elastic scattering data available in the EXFOR library [10]. The name of the first author, the year of publication, the neutron energy range under study, the quantity (CS and/or DA), and the number of points are listed.

Reference		E_n range (MeV)	Quantity (Points)	
Rodgers (1967)	[12]	2.33	CS(1)	DA(5)
Boschung (1971)	[13]	4.04–5.60	CS(3)	DA(30)
Fedorov (1973)	[14]	2.90		DA(8)
Kinney (1974)	[15]	5.50–8.50	CS(3)	DA(62)
Korzh (1977)	[16]	1.50–3.00	CS(4)	DA(35)
El-Kadi (1982)	[17]	7.96–13.90	CS(4)	DA(105)
Korzh (1987)	[18]	5.00–7.00	CS(3)	DA(39)
Guenther (1989)	[19]	1.30–3.97		DA(370)
Vanhoy (2018)	[20]	2.00–6.00		DA(121)

6 MeV, accurate experimental data in this region are the only way to sufficiently constrain the uncertainties on the current evaluated data files of iron.

Even though natural iron and ^{56}Fe are among the most measured materials, experimental data for the minor isotopes are limited. In the case of elastic scattering on ^{54}Fe, only a handful of experimental data are available in the EXFOR [10] library for neutron incident energies higher than 1 MeV (Table I). On the one hand, for the elastic scattering cross section (CS), only a few scattered points are available in the energy range from 1 to 8 MeV, measured with quasimonoenergetic neutron beams. In some cases the uncertainties of these values reach 17% and discrepancies between the different data sets are also observed. On the other hand, the differential cross section with respect to angle (DA) has been measured only for a small number of neutron energies.

For inelastic scattering, several experimental data are available in EXFOR, based on either neutron or γ spectroscopy. In Table II the data sets that correspond to the partial cross section (CSP) and differential cross section (DAP) from the first excited state of ^{54}Fe ($E_x = 1.408$ MeV) are listed. Only a few of these experiments produced inelastic cross sections for energies higher than 4 MeV, mostly experiments based on neutron spectroscopy, since γ spectroscopy is affected by the not so well known level scheme of ^{54}Fe [11] above this energy, resulting in unknown levels feeding the first excited state and thus affecting the subsequent deexcitation via the emission of the 1.408 MeV γ ray.

For the above mentioned reasons, new experimental data on scattering cross sections are crucial for clearing out discrepancies between experimental data, lowering uncertainties on the current evaluated libraries of iron, and finally assisting in the development of optical models used for predicting cross sections of iron isotopes. The aim of this work is to produce, for the first time, high-resolution cross sections and neutron angular distributions for both elastic and inelastic scattering on ^{54}Fe in the fast neutron energy region (1 to 8 MeV), using a highly enriched sample, a white neutron source coupled with the time-of-flight technique, and a detection setup consisting of liquid organic scintillators for an accurate neutron spectrometry.

TABLE II. Partial inelastic scattering cross sections from the first excited level of ^{54}Fe, available in EXFOR [10]. The name of the first author, the year of publication, the neutron energy range under study, the quantity (CSP and/or DAP), and the number of points are listed

Reference		E_n range (MeV)	Quantity (Points)	
Rodgers (1967)	[12]	2.33	CSP(1)	DAP(5)
Tsukada (1969)	[22]	2.65–3.26	CSP(1)	DAP(22)
Boschung (1971)	[13]	4.04–5.60	CSP(14)	DAP(29)
Fedorov (1973)	[14]	2.90	CSP(1)	DAP(8)
Kinney (1974)	[15]	5.50–8.50	CSP(3)	DAP(64)
Almen-Ramström (1975)	[23]	2.50–4.50	CSP(9)	
Korzh (1977)	[16]	2.00–3.00	CSP(3)	DAP(27)
El-Kadi (1982)	[17]	7.96–13.9	CSP(4)	DAP(104)
Guenther (1986)	[19]	1.30–3.97	CSP(60)	
Korzh (1987)	[18]	5.00–7.00	CSP(3)	DAP(39)
Mittler (1987)	[24]	1.46–3.69	CSP(29)	
Olacel (2018)	[25]	1.41–18.00	CSP(326)	
Vanhoy (2018)	[20]	2.25–6.00		DAP(107)

II. EXPERIMENTAL CONDITIONS

The experiments were carried out at the GELINA neutron time-of-flight facility of the JRC-Geel [21]. The facility consists of an electron linear accelerator, a neutron producing target, and flight paths where the various experimental setups are installed. Short electron bursts of 2 ns duration are impinging on a depleted uranium disk (neutron producing target), producing photons via the bremsstrahlung process and then neutrons through photonuclear (γ, n), (γ, f) reactions in the uranium nuclei. The primary neutrons have an evaporation spectrum and are emitted isotropically. They enter the flight path either directly (DFC, direct flux configuration) or after moderation (MFC, moderated flux configuration). Here the direct flux configuration was used, supplying a neutron beam with energies from 100 keV to almost 10 MeV.

The experimental setup used in this work is placed at flight path 1, at 108° with respect to the electron beam direction. The sample is placed 27.037 m away from the neutron source. Inside the flight tube a collimation system is installed to define the size of the beam. The collimators consist of layers of specially chosen materials absorbing different components of the beam. These materials are lithium epoxy for the absorption of slow neutrons, copper for fast neutrons, and lead for photons. Furthermore, two filters, one made out of depleted uranium and the other one out of boron carbide, are placed in the flight path tube, at the exit of the target hall, in order to minimize the intensity of the bremsstrahlung and the thermal neutron component. The beam size was measured at the sample position using a photographic film, resulting in 4.9(2) cm diameter.

The highly enriched ^{54}Fe sample used in the present work was leased from the Isotope Office of Oak Ridge National Laboratory. The isotopic composition and the geometrical characteristics of the sample are listed in Table III. The estimated areal density of the ^{54}Fe sample was 0.954 g/cm^2 with a 2% uncertainty.

TABLE III. Properties of the ^{54}Fe sample. Isotopic composition and geometrical characteristics.

Fe isotope	^{54}Fe	^{56}Fe	^{57}Fe	^{58}Fe
Abundance (%)	97.68(7)	2.24(6)	0.04(1)	0.04(1)
Mass (g)		19.494(10)		
Diameter (mm)		51.00(51)		
Thickness (mm)		1.30(1)		
Molar mass (g/mol)		53.987(2)		
Density (g/cm^2)		0.954(18)		

Two types of measurements were performed. One with the sample in the beam (sample-in), that lasted almost 360 hours, and a second one without the sample (sample-out) for a duration of 330 hours. The sample-out measurement was carried out in order to determine the background contribution from in-beam neutrons that scattered once or multiple times in the air and surrounding materials and then got detected by one of the scintillators.

III. THE ELISA SPECTROMETER

For the detection of the scattered neutrons, the ELastic and Inelastic Scattering Array (ELISA) was used [26–28]. The spectrometer consists of two main parts: 32 liquid organic scintillators for the detection of the scattered neutrons, and a ^{235}U fission chamber for the measurement of the neutron flux. The setup is designed for the measurement of elastic and inelastic scattering cross sections and angular distributions.

Two different types of commercially available liquid organic scintillators, manufactured by Scionix, are used. Half of the detectors (model 51A51/2MQOE1-EJ301-NX) use the EJ301 scintillator material (NE213 equivalent) [29] and the other half use the EJ315 one (model 51A51/2MQOE1-EJ315-NX; C_6D_6 type) [30]. The detectors have a cylindrical shape with a liquid cell of 5.08 cm height and of 2.54 cm radius, filled up to 97% with the corresponding hydrocarbon liquid. These are fast scintillators with a time resolution below 1 ns. They are suitable for neutron spectrometry since photon/neutron separation can be achieved via pulse shape analysis. The reason behind using two different types of detectors, hydrogen (EJ301) and deuterium (EJ315) based, is that the detected neutrons create two different pulse height responses which provides a cross-check between the two types, which assists in the discovery of systematic errors during the data analysis. In the ELISA setup (Fig. 1), the scintillators are split into four sets of eight detectors each, mounted at specific angles with respect to the neutron beam direction (Table IV). The detection angles have been carefully chosen so that their corresponding cosines match the zeros of the Legendre polynomial of the eighth order. This allows the calculation of the integral cross section σ using the Gauss-Legendre quadrature rule

$$\sigma = 2\pi \sum_{i=1}^{8} w_i \frac{d\sigma}{d\Omega}(\cos\theta_i), \tag{1}$$

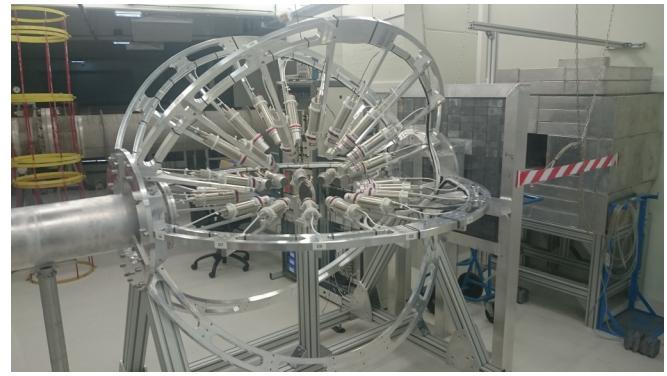

FIG. 1. The ELISA spectrometer. The neutron beam comes from the right, passing through the fission chamber located behind the lead wall and then it reaches the scattering sample. Here the lead wall acts as the last collimator.

where $\frac{d\sigma}{d\Omega}(\cos\theta_i)$ is the differential cross section as a function of the scattering angle θ_i, and w_i are the corresponding weight factors (Table IV).

The data acquisition system used for the scintillators is a digitizer based system consisting of eight cards with four input channels each. They are commercially available digitizers manufactured by SP Devices (model ADQ14DC-4A-VG-PXIe). They have a 14-bit amplitude resolution and 500 MS/s sampling rate (where MS denotes 10^6 samples). For the synchronization of the digitizer clocks an external 10 MHz reference is provided by a clock generator. The acquired data, i.e., waveforms and their corresponding timestamps are saved for offline processing.

The fission chamber contains a set of eight UF_4 deposits on five aluminum foils of 84 mm diameter and 20 μm thickness. The deposits were manufactured at the JRC-Geel, using the evaporation technique. The isotopic composition of the material used for the manufacturing of the deposits is presented in Table V. The diameter of the deposits is 70 mm, determined by the evaporation mask that was used. The total areal density of ^{235}U was experimentally determined by alpha counting and it was found to be 4095(4) μg/cm^2. Two single-sided foils are placed in the front and the back of the chamber,

TABLE IV. Detection angles with respect to the neutron beam direction, the calculated cosines, and the corresponding weights used for the implementation of the Gauss-Legendre quadrature rule. The uncertainty of the detection angles represents the accuracy in the construction of the frame supporting the detectors.

#	Angle (deg)	Cosine	Weight
1	163.8 (1)	−0.9603 (5)	0.1012
2	142.8 (1)	−0.7967 (11)	0.2224
3	121.7 (1)	−0.5255 (15)	0.3137
4	100.6 (1)	−0.1834 (17)	0.3627
5	79.4 (1)	0.1834 (17)	0.3627
6	58.3 (1)	0.5255 (15)	0.3137
7	37.2 (1)	0.7967 (11)	0.2224
8	16.2 (1)	0.9603 (5)	0.1012

TABLE V. Isotopic composition of the UF_4 primary material.

U isotope	^{233}U	^{234}U	^{235}U	^{236}U	^{238}U
Abundance (%)	0.001	0.036	99.94	0.011	0.013

facing forward with respect to the neutron beam, and three double-sided foils are placed in the middle, each with a 14 mm distance between them. Each deposit faces the corresponding anode, i.e., a 25 μm thick aluminum electrode, placed at a distance of 7 mm for the recording of the fission fragments. The fission chamber is filled with P10 gas at atmospheric pressure.

The data acquisition system used for the fission chamber is based on nuclear instrumentation module (NIM electronics). First, the recorded signals pass through a charge integrating preamplifier (CSTA2HV) and then are split in two directions. In one direction, the signal passes through a spectroscopic amplifier (Ortec 671) and from there continues to an analog-to-digital converter (ADC, FAST ComTec 7072). In the other direction, the signal passes first through a fast filter amplifier (Ortec 579), then a constant fraction discriminator (CFD, Ortec 584), and ends up at a time-to-digital converter (TDC, developed at the JRC). The information coming from the ADC and the TDC are synchronized in time for each incoming signal using a multiplexer (MMPM, developed at the JRC) and gets stored for offline analysis.

IV. ANALYSIS

A detailed description of the core of the analysis procedure for data obtained with the ELISA spectrometer is given in [31], here only a short presentation of the most important parts is given.

The first step of the data analysis is processing of the signals recorded by the scintillators. For every produced waveform the total integrated charge (light output equivalent) and the corresponding time stamps are extracted. A correction is implemented to the time stamps, to improve the time resolution using the constant fraction discrimination (CFD) algorithm [32–34]. To distinguish neutrons from photon induced events short (Q_S) and long (Q_L) intervals of the signal are made (Fig. 2). The pulse shape discrimination (PSD) factor is defined as the ratio of the integral of the tail (Q_L–Q_S) to the long interval (Q_L). In Fig. 3, the resulting pulse shape discrimination spectrum is presented with respect to the light output, for one of the EJ301 detectors [35–37].

Once all signals are processed, the next step is the characterization of the detector's response function $R(L, E)$, which represents the probability of a particle with an energy E producing a light pulse with amplitude L. The method followed in the present work was a combination of measurement and Monte Carlo simulation as described in [38–41]. The characterization of the detectors is repeated for every different experimental campaign at the ELISA spectrometer, in order to monitor the stability of the detectors and identify problems that might have occurred during the measurements. First, a set of calibration measurements using γ-ray

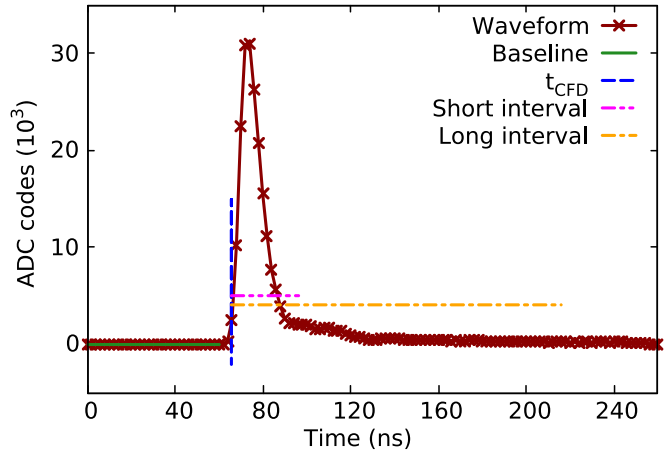

FIG. 2. Example of a recorded signal. The time correction based on the CFD algorithm, along with the intervals for the pulse shape discrimination are presented.

sources were performed. The sources that were used and their properties are presented in Table VI. They were placed in the sample position of the spectrometer, 29.5(1) cm away from the detectors. Then, detailed Monte Carlo simulations of these measurements were carried out. To this end, the MCNP6.2 [42,43] code was used. A detailed description of the geometry of the detectors was given as input and the sources were defined as isotropic with the same properties and geometrical characteristics as the ones used in the actual measurements. The light output distributions produced by each source from the simulations were then folded with the resolution function given in [31] and fitted to the corresponding experimental light output histograms. Via this fit, the parameters for the resolution function for each detector were obtained.

For the neutron response, the non-linear behavior of the light output produced by charged particles heavier than the electron, in the present case protons (EJ301) and deuterons

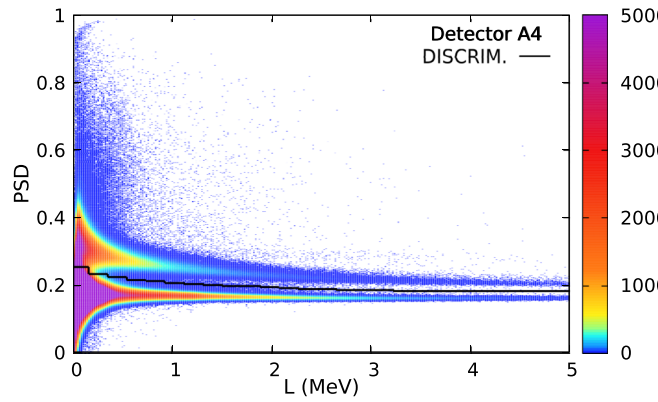

FIG. 3. The two-dimensional pulse shape discrimination (PSD) spectrum as a function of the light output (L) for one of the EJ301 detectors. The black line (DISCRIM.) represents the optimal separation point between neutron (upper part) and photon (lower part) induced events.

TABLE VI. Characteristics of the γ-ray sources. The half-life, the activity, the energy of the emitted γ rays, and the corresponding energy of the Compton edge are given for each isotope.

Source	$T_{1/2}$ (yr)	A_d (kBq)	E_γ (keV)	E_c (keV)
^{137}Cs	30.05	365.57	662	477
^{207}Bi	32.90	359.78	570	394
			1064	858
			1770	1547
^{22}Na	2.61	139.22	511	341
			1275	1062
^{232}Th	1.4×10^{10}	N.A.	2615	2382
AmBe	432.60	N.A.	4438	4196

(EJ315) needs to be considered. In the present work, the empirical formula

$$L(E_r) = A_1 E_r + \frac{A_2 E_r^2}{E_r + A_3}, \tag{2}$$

provided by Kornilov *et al.* [40], was used for the description of the light output distributions, where E_r is the recoil energy of the charged particle, and A_1, A_2, A_3 are parameters determined for each detector individually. These parameters can only be determined experimentally. For that, a dedicated experiment was performed at the ELISA spectrometer using a natural carbon sample. Carbon was chosen for its high inelastic threshold of 4.81 MeV, meaning that below this energy only neutrons that are scattered elastically arrive at the detectors. Short time-of-flight intervals of 5 ns, that correspond to narrow energy ranges, were selected, and for each one of these neutron energies the corresponding simulated light output distribution was fitted to the experimental one. In the end, the different parameters obtained from each energy were fitted to extract a set of values that would work best for the whole neutron energy range. With this method, a model describing the response function was developed for each detector individually. This model was then implemented in the ^{54}Fe data analysis, an example of which is presented in Fig. 4. After acquiring the neutron time-of-flight spectra for each detector the background contribution needs to be extracted. In the current experiment, background related events are generated when beam neutrons interact one or more times in the air and surrounding materials and then arrive in the detectors. To account for this contribution, a measurement without the sample was performed and was subtracted from the one with the sample in place. To account for the difference in measurement time between sample-in and sample-out measurements, a normalization factor was calculated based on the fission events recorded in the ionization chamber. On average the background component accounted for 40% of the recorded events in each detector. Following the removal of photon induced events and the background contribution, the separation between events coming from elastic and inelastic scattering took place. To do that, each time-of-flight spectrum was split in small intervals of 5 ns duration and their corresponding light output distributions were analyzed. In Fig. 4 examples of such light output distributions are presented for both type of detectors placed at four different detection angles. In this case the time-of-flight (t.o.f.) interval (1060 to 1065 ns) corresponds to an incident neutron energy range from 3.47 to 3.50 MeV. Via kinematic calculations, it is possible to determine the energy of the neutron that was scattered elastically $E_{\rm el}$ or inelastically $E_{\rm inl}$ for every t.o.f. interval. These

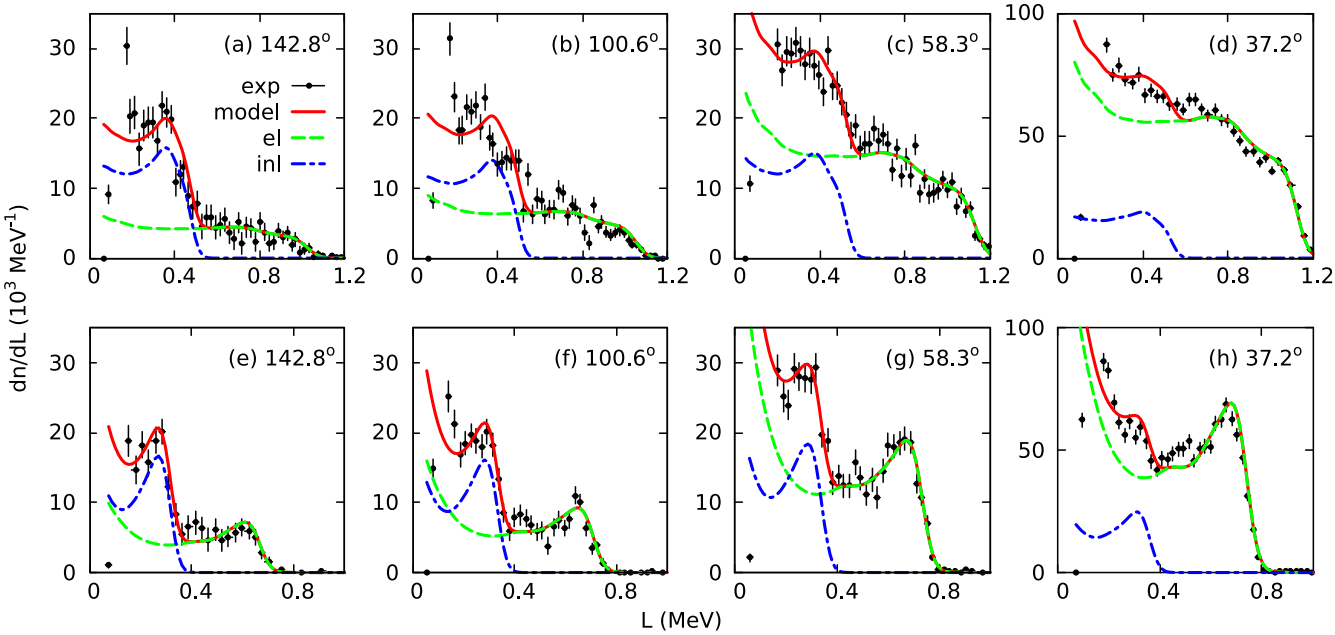

FIG. 4. Light output distributions for the time-of-flight interval from 1060 to 1065 ns. The graphs correspond to four different detection angles for both the EJ301 (n, p) [(a) to (d)] and EJ315 (n, d) [(e) to (h)] detectors. The experimental values (exp) are presented along with their associated response (model) and their different components from elastic scattering (el) and inelastic scattering (inl) from the first excited stated of ^{54}Fe (1.408 MeV).

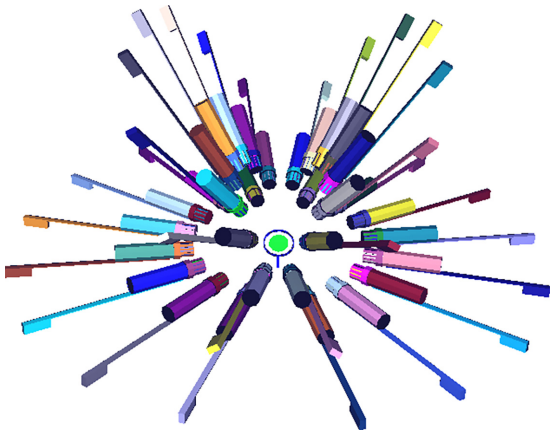

FIG. 5. MCNP version of the ELISA spectrometer. In the geometry, the sample holder, the ^{54}Fe disk, the 32 liquid organic scintillators, and their respective mounting are included.

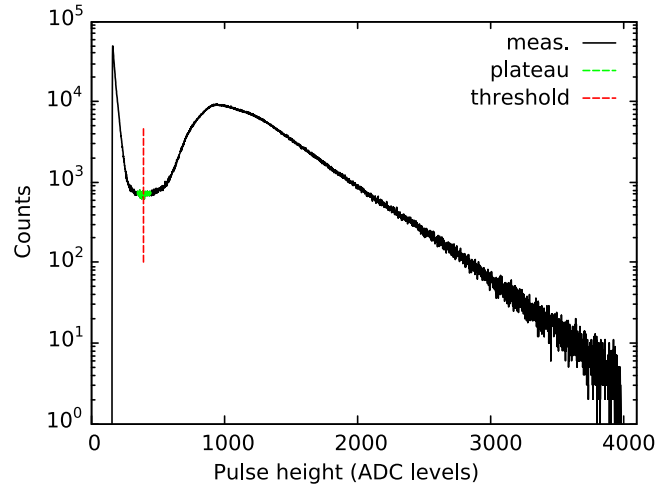

FIG. 6. Full pulse height histogram of the ^{54}Fe sample-in measurement. The experimental counts (black) are presented along with the corresponding threshold (red) and the plateau region (green) that was used for the linear fit.

two different neutron energies generate different light output distributions that overlap as seen in Fig. 4. For the elastic scattering, a threshold is applied to cut out contribution from inelastic scattering induced events. This threshold is placed at the maximum light output produced by an inelastic event taking into account the resolution broadening of the detector and is calculated using Eq. (2). The detector's modeled response $R(L, E_{\rm el})$ for neutrons with energy $E_{\rm el}$ is scaled by a factor (λ) to match the experimental data above the threshold, and the resulting distribution $R_{\rm fit}(L, E_{\rm el}) = \lambda\, R(L, E_{\rm el})$ describes the contribution of elastic scattering events to the total light output distributions. The number of elastic scattering events is then extracted using

$$N_{\rm el}({\rm t.o.f.}, \theta) = \frac{1}{\epsilon(E_{\rm el})|_{L_{\rm thr}}\,\Delta\Omega} \int_{L_{\rm thr}} R_{\rm fit}(L, E_{\rm el})dL, \qquad (3)$$

where $N_{\rm el}$ is the number of elastic scattering events per 5 ns t.o.f. interval and detection angle, $\Delta\Omega$ is the detector opening angle, and $\epsilon(E_{\rm el})|_{L_{\rm thr}}$ is the efficiency of each detector as a function of the detected neutron energy $E_{\rm el}$ calculated for the threshold value $L_{\rm thr}$ using $\epsilon(E_{\rm el})|_{L_{\rm thr}} = \int_{L_{\rm thr}} R(L, E_{\rm el})dL$. The same procedure was followed for the inelastic scattering events coming from the first exited state of ^{54}Fe, by applying the appropriate threshold for the second excited state and subtracting the contribution of the elastic scattering events.

The obtained numbers of neutron induced events for the different scattering processes were corrected for multiple scattering effects before being used in the cross section calculation. The multiple scattering contribution is generated from beam neutrons that interact two or more times in the ^{54}Fe sample and then reach one of the detectors. In the present work, the correction factor for such events ($f_{\rm msc}$) was calculated via Monte Carlo simulations using the MCNP6.2 code. In the simulation, the full geometry of the spectrometer was given as input (Fig. 5), and the description of the neutron source was based on the actual properties of the beam during the measurement. The PTRAC option of MCNP was selected as output where the history of each neutron arriving in any of the detectors is recorded. Then, the number of neutron events that interacted more than once with the sample and then arrived at any detector was written down, and the correction factor was defined as the ratio of the detected multiple scattering events to the total number of detected events. This method provides a time-of-flight dependent correction for every detector individually and is applied to the differential scattering yield using

$$N'_{\rm el/inl}({\rm t.o.f.}, \theta) = (1 - f_{\rm msc})N_{\rm el/inl}({\rm t.o.f.}, \theta), \qquad (4)$$

where $N_{\rm el/inl}$ is the initial number of elastic/inelastic scattering events per 5 ns t.o.f. interval and detection angle, and $N'_{\rm el/inl}$ is the final number of elastic/inelastic scattering events. With the PTRAC option of MCNP the isotope with which the neutrons interacted is also recorded, which also allows for the identification of events that interacted with the other Fe isotopes in the sample and then reached any of the detectors. The same method as the one for the multiple scattering contribution [Eq. (4)] was followed to correct for the contamination of the minor Fe isotopes in the ^{54}Fe sample. This contamination factor ($f_{\rm con}$) was found to be less than 1% of the recorded neutron events at each detection angle over the whole neutron energy region.

Once the scattering yields have been determined, the neutron fluence impinged on the ^{54}Fe sample needs to be calculated. This is achieved by analyzing the ionization chamber data. The neutron fluence is extracted using the standard cross-section of the neutron induced fission on ^{235}U and is determined using [44]

$$\Phi(E) = \frac{Y_{\rm FC}(E)}{\epsilon_{\rm FC}\,\sigma_{^{235}{\rm U}(n,f)}\,\rho_{^{235}{\rm U}}\,A_b}, \qquad (5)$$

where $Y_{\rm FC}(E)$ is the total number of fission fragments above threshold (Fig. 6) as a function of the neutron energy E, $\epsilon_{\rm FC}$ is the detection efficiency of the fission chamber, $\sigma_{^{235}{\rm U}(n,f)}$ is the neutron induced fission cross section of ^{235}U, $\rho_{^{235}U}$ is the areal

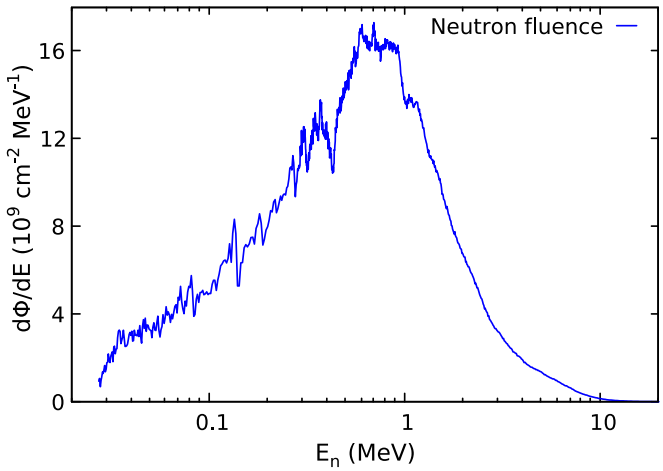

FIG. 7. Neutron fluence impinged on the ^{54}Fe sample with respect to the neutron incident energy. It corresponds to the total duration of the sample-in measurement that amounts to 360 hours.

density of the ^{235}U deposits in atoms per unit surface, and A_b is the cross-sectional area of the neutron beam. The detection efficiency was determined using

$$\epsilon_{\mathrm{FC}} = \frac{Y_{\mathrm{FC}}}{Y_{\mathrm{FC}} + Y_A + Y_B}, \tag{6}$$

where Y_A is the number of fission fragments below the threshold, determined with a linear fit of the counts in the plateau region and extrapolating to zero amplitude, and Y_B is the number of fission fragments that were stopped in the ^{235}U deposits, determined using the method described in [45]. The resulting neutron fluence for the sample-in measurement is presented in Fig. 7.

TABLE VII. Systematic uncertainties of the ^{54}Fe data analysis.

Contribution	Uncertainty
Sample areal density	2%
Fission chamber efficiency	1%
^{235}U(n, f) cross section	1.1–1.2%
^{235}U deposits mass	0.001%
Multiple scattering correction	4–6%
Contamination of minor Fe isotopes	<1%

Upon the determination of all the different components, the differential cross section was calculated using

$$\frac{d\sigma}{d\Omega}(E,\theta)_{\mathrm{el/inl}} = \frac{N'_{\mathrm{el/inl}}(E,\theta)}{\Delta\Omega\,\Phi(E)\rho_T A_b}, \tag{7}$$

where E is the neutron incident energy, $N'_{\mathrm{el/inl}}$ is the corrected number of elastic/inelastic scattering events, $\Delta\Omega$ is the detector's solid angle, $\Phi(E)$ is the neutron fluence, ρ_T is the areal density of the ^{54}Fe sample, and A_b is the cross-sectional area of the neutron beam, which is canceled out by combining Eqs. (5) and (7). Then the angle-integrated cross section was calculated using Eq. (1). The corresponding total uncertainty of the resulting cross section was calculated by uncertainty propagation using the root-sum-square method, taking into account all individual contributions. In principle the final uncertainty was extracted by calculating the square root of the sum of the squares of the partial derivatives multiplied by the corresponding uncertainties. The statistical uncertainty of the cross section results from the number of scattered neutrons from the ^{54}Fe sample that arrived in the detectors and the fission fragment yield of the ^{235}U deposits. The various systematic contributions in the data analysis are presented in Table VII.

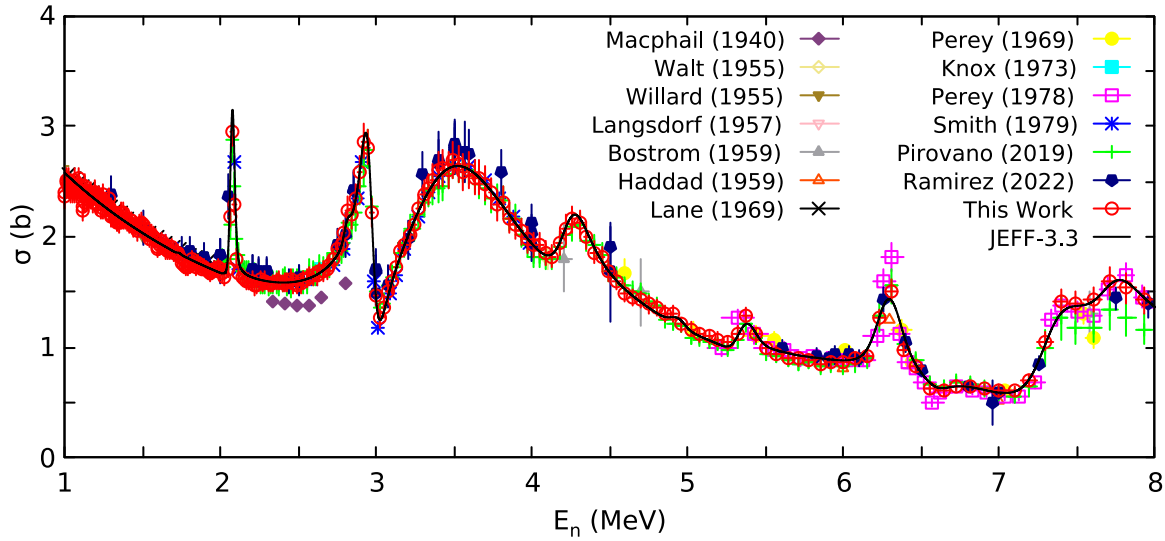

FIG. 8. Angle-integrated cross section of neutron elastic scattering on $^{\mathrm{nat}}$C as a function of the neutron incident energy compared to other experimental data available in the EXFOR library [10,46–57], and the JEFF-3.3 evaluation [4] folded with the experimental energy resolution of the measurement.

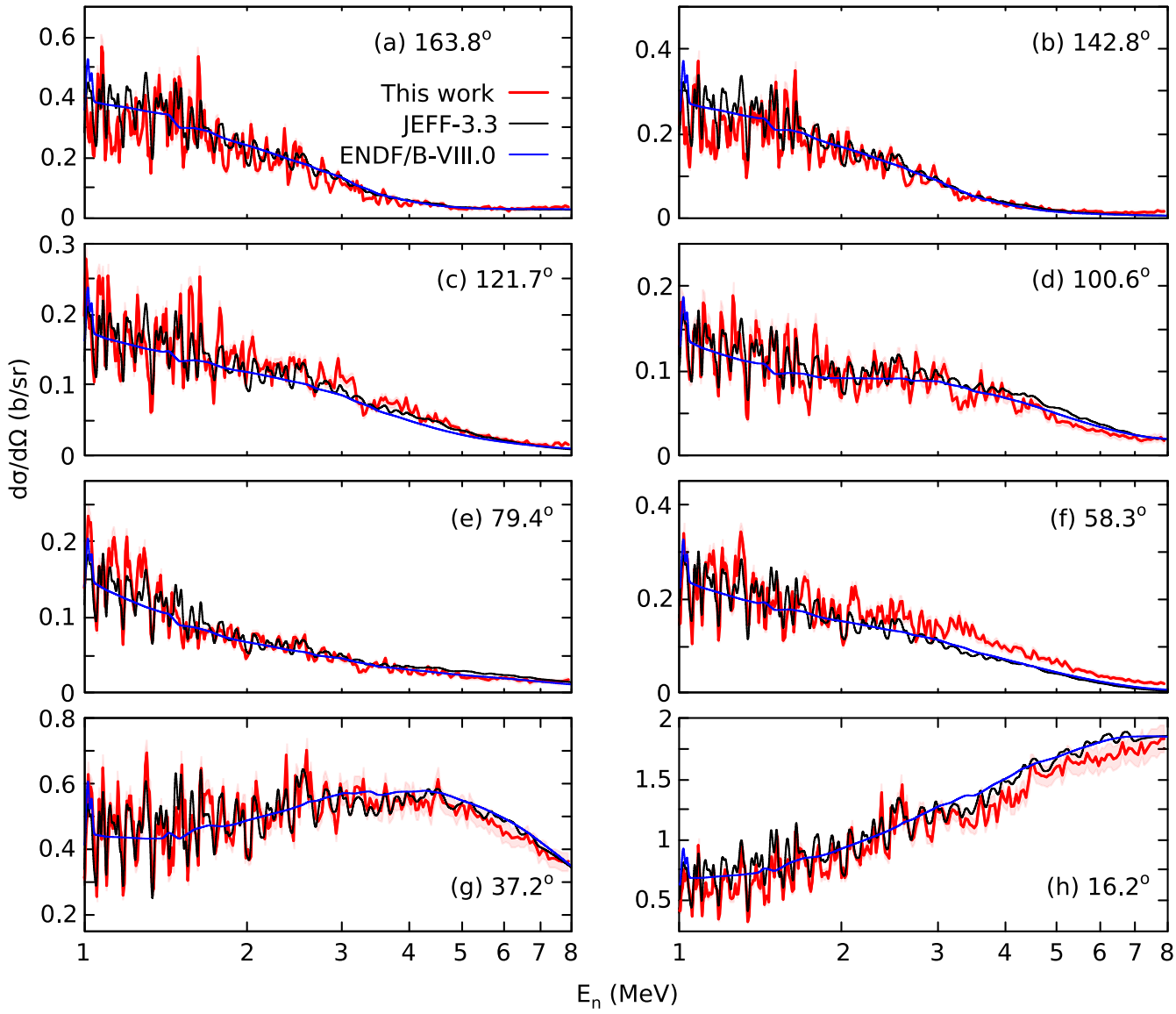

FIG. 9. Differential cross sections of neutron elastic scattering on ^{54}Fe as a function of the neutron incident energy at eight detection angles. The experimental cross sections are compared with the evaluated values provided by JEFF-3.3 [4] and ENDF/B-VIII.0 [58] folded with the experimental energy resolution. The experimental total uncertainties are shown with shadow bars.

V. VALIDATION OF THE ANALYSIS

For the validation of the whole analysis procedure, the cross section of neutron scattering by a purely scattering natural carbon sample was calculated. As mentioned above, a dedicated experiment was performed at GELINA with the ELISA spectrometer using a natural carbon sample, in order to determine the parameters of the light output function [Eq. (2)] used in the neutron response models. Carbon is a very well suited candidate for this validation since the differential cross section of neutron elastic scattering by carbon is a standard for $E_n \leqslant 1.8$ MeV and the elastic scattering cross section is well known up to 6.45 MeV neutron energy with an uncertainty of $\leqslant 1\%$ [59].

The scattering sample that was used in the experiment was a 27.70(1) g graphite disk with 2 mm thickness and 100 mm diameter. The calculated areal density of the sample was 1.761(3) g/cm^3. The experiment lasted almost 600 hours: 360 hours of sample-in and 240 hours of sample-out measurements. The total integrated neutron elastic scattering cross section is shown in Fig. 8 along with the JEFF-3.3 evaluation, and the available data in the literature. The cross section of elastic scattering by carbon has sharp resonances at 2.816 and 4.937 MeV neutron energies that were not resolved with the current energy resolution of the spectrometer. In response to that, the JEFF-3.3 evaluation was folded with the experimental resolution. The results obtained with the ELISA spectrometer are compatible within uncertainty with the values given in the JEFF-3.3 evaluation over the whole neutron energy range. The total uncertainty of the values varies from 3% to 8% and is mainly due to the statistics of the experiment.

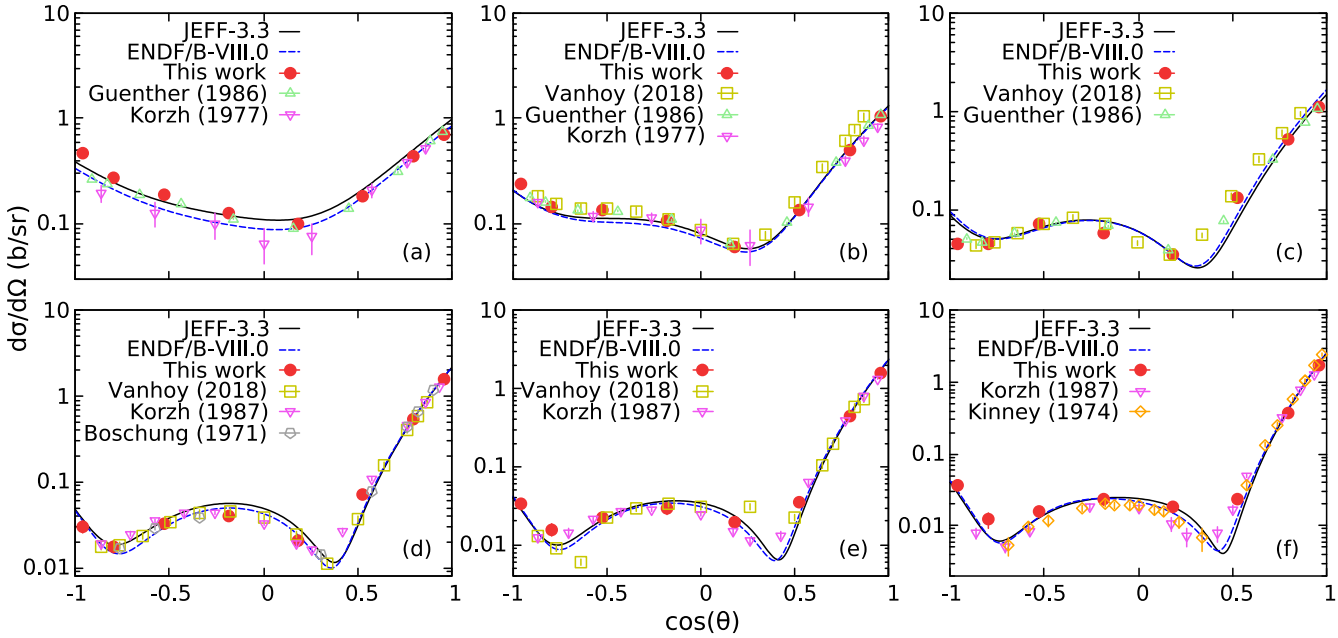

FIG. 10. Comparison of differential cross sections of neutron elastic scattering on ^{54}Fe as a function of the cosine of the scattering angle θ, with data available in literature and the angular distributions provided in the JEFF-3.3 and ENDF/B-VIII.0 evaluations [4,58]. Six t.o.f. intervals of 5 ns have been selected, that correspond to the following neutron energy ranges: (a) $E = 1.494$–1.503 MeV, (b) $E = 2.493$–2.513 MeV, (c) $E = 3.499$–3.532 MeV, (d) $E = 4.973$–5.030 MeV, (e) $E = 5.938$–6.012 MeV, (f) $E = 6.929$–7.023 MeV.

The agreement between the experimentally determined cross section and the evaluated values demonstrates that the response function models that were developed in the framework of this analysis and then used in the ^{54}Fe data are able to properly reproduce the experimental light output distributions.

VI. ELASTIC SCATTERING CROSS SECTION

The results for the differential cross section of neutron elastic scattering on ^{54}Fe are presented in Fig. 9 with respect to the incident neutron energy for eight different detection angles, in the energy range from 1 to 8 MeV. The results are compared with the values provided by the JEFF-3.3 and ENDF/B-VIII.0 [58] evaluations folded with the experimental energy resolution. For the evaluated differential cross sections, ENDF/B-VIII.0 has adopted optical model calculations, above 1 MeV neutron incident energy, produced by the EMPIRE nuclear reaction code [60], while JEFF-3.3 used a Legendre representation for energies below 20 MeV, based on the sum of calculated Legendre coefficients for compound nucleus and shape-elastic scattering. The difference between the adopted methods of the evaluations explain the difference in the shape of the resulting cross sections, where the ENDF/B-VIII.0 cross sections are following a smooth trend, while the JEFF-3.3 cross sections have a fluctuating behavior. There is an overall good agreement between experimental and evaluated values over the whole neutron energy range. Only in the case of 58.3°, for energies approximately above 2 MeV, is the experimental cross section systematically higher than the values proposed by the evaluation. The same issue was also observed in [26], in a comparison of experimental differential cross section of neutron elastic scattering on ^{nat}Fe at 58.3° and evaluated values proposed by ENDF/B-VIII.0. Meanwhile, in the case of the ^{nat}C(n, n) validation measurement the resulting cross section at 58.3° was in good agreement with the well known evaluated values, so this consistency between ^{54}Fe and ^{nat}Fe at 58.3° indicates possible issues with the evaluations of neutron angular distributions on Fe isotopes. For the differential cross sections the total uncertainties vary from 5% to 25%, and are mainly generated from the duration of the experiments and their related statistics. The highest uncertainties, above 15%, are observed in the energy range between 6 and 8 MeV at backward angles, where the cross section is reaching very low values due to the fact that elastic scattering on Fe is a forward-peaked reaction.

In Fig. 10, the differential cross section is given as a function of the cosine of the detection angle θ. The data are compared with values available in the EXFOR library and the angular distributions provided by the JEFF-3.3 and ENDF/B-VIII.0 evaluations. Six t.o.f. intervals of 5 ns have been selected, that cover most of the neutron incident energies measured in other experiments reported in EXFOR (Table I). In general, there is a satisfactory agreement between the cross section values calculated in this work and the experimental data available in literature. The results are in agreement with the latest measurement performed by Vanhoy *et al.* [20] using quasimonoenergetic neutron beams. Also, in the energy intervals above 2.5 MeV for the cosine that corresponds to the 58.3° (0.5255) detection angle, it is observed again that the cross section values calculated in this work are higher than the ones reported in JEFF-3.3, and ENDF/B-VIII.0 evaluations, but values from other experiments also support higher cross sections in this region.

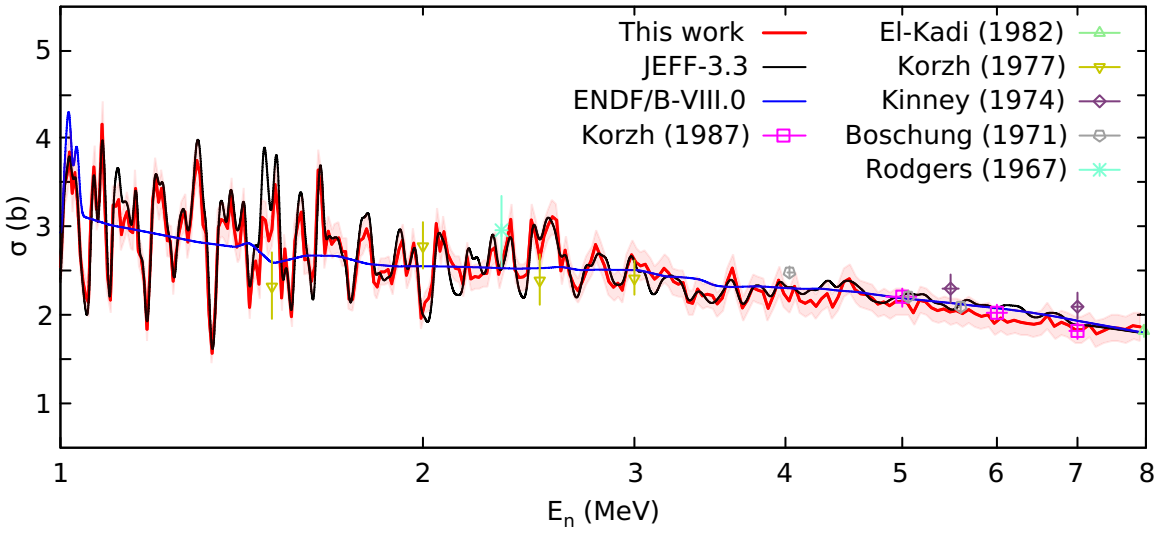

FIG. 11. Angle-integrated cross section of neutron elastic scattering on ^{54}Fe as a function of the neutron incident energy compared with data available in the EXFOR library [10], and the JEFF-3.3 and ENDF/B-VIII.0 evaluations [4,58] folded with the experimental energy resolution of the measurement.

The angle-integrated neutron elastic scattering cross section is presented in Fig. 11. The results are compared with the data available in the literature, JEFF-3.3 and ENDF/B-VIII.0 evaluations folded with the experimental resolution of the measurement. In the JEFF-3.3 evaluation, the elastic scattering cross section was calculated by subtracting the optical model based nonelastic cross section from the evaluated total cross section, which was purely based on the experimental data of Carlton *et al.* [61], while the ENDF/B-VIII.0 evaluated values were produced using the EMPIRE code. The results of this work are in overall good agreement with the few previous experimental values available in the EXFOR library and the JEFF-3.3 and ENDF/B-VIII.0 evaluations, especially in the energy region between 1 and 3 MeV where resonances are causing big fluctuations in the cross section. This agreement validates the evaluation methodology employed in JEFF-3.3, which involved the combination of high-resolution transmission data and optical model calculations to extract the elastic scattering cross section. The total uncertainty of the angle-integrated cross section varies between 5% and 8%.

VII. INELASTIC SCATTERING CROSS SECTION

The results for the differential cross section of neutron inelastic scattering from the first excited state of ^{54}Fe (1.408 MeV), in the energy range from 2.5 to 5.5 MeV, are presented in Fig. 12. The cross sections are given with respect to the neutron incident energy at eight different detection angles. The values are compared with the ENDF/B-VIII.0 evaluated library, which is based on optical model calculations using the EMPIRE code. For most of the detection angles the measured values are slightly higher than the ones provided by ENDF/B-VIII.0 over the whole neutron energy range. The total uncertainties range from 7% to 50%. Just as in elastic scattering, high uncertainties, above 20%, are observed in the two forward detectors for energies above 4 MeV. The reason for that is the fact that the inelastic scattering yield is extracted after the subtraction of the elastic scattering component in the corresponding light output distribution (see Fig. 4). At these angles, the inelastic scattering cross section is decreasing but the elastic scattering one is increasing with the neutron energy, reaching values 20 times higher than the inelastic scattering one, making it the predominant reaction in this energy range. In this case, the only way to lower the uncertainties is by performing much longer measurements.

In Fig. 13 the differential cross section is presented as a function of the cosine of the detection angle θ, and compared with data available in the literature and the ENDF/B-VIII.0 evaluation. Similarly to elastic scattering, six t.o.f. intervals of 5 ns have been selected, covering again most of the neutron incident energies that have been measured in other experiments reported in EXFOR (Table II). In the first three t.o.f. intervals [(a) to (c)], even though discrepancies are observed between the results and the experimental values from the EXFOR library, there is a relatively good agreement between the cross sections calculated in this work and the values provided by the ENDF/B-VIII.0 evaluation. In the remaining t.o.f. intervals [(d) to (f)] the results are systematically higher than ENDF/B-VIII.0, but in agreement within uncertainty with the other experimental values, over all detection angles.

The angle-integrated neutron inelastic scattering cross section from the first excited state of ^{54}Fe is presented in Fig. 14 in the energy range from 2.5 to 5.5 MeV. The total uncertainty of the cross section varies between 6% and 20%. The results are compared with the data available in the literature, JEFF-3.3 and ENDF/B-VIII.0 evaluations. It is observed that the results are following the trend of the evaluation values, with a good agreement within uncertainty with JEFF-3.3, which proposes slightly higher cross section values than ENDF/B-VIII.0. In comparison with the other experimental

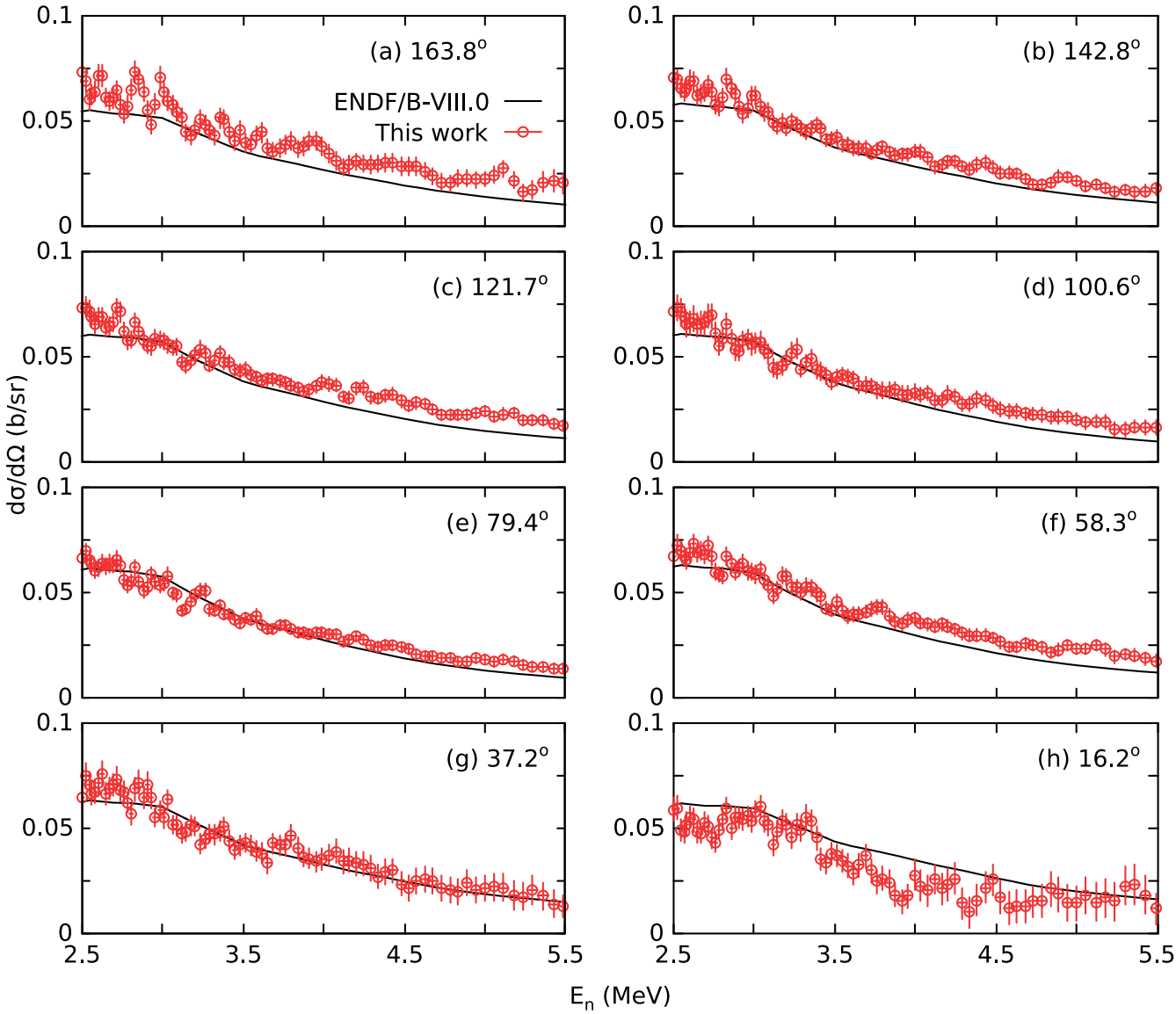

FIG. 12. Differential cross sections of neutron inelastic scattering from the first excited state of ^{54}Fe as a function of the neutron incident energy at eight detection angles. The experimental cross sections are compared with the evaluated values provided by ENDF/B-VIII.0 [58].

values reported in the EXFOR library, there is an overall good agreement within uncertainty with almost all experiments. It is worthwhile to mention that between 3 and 4.5 MeV neutron energies the results are in agreement within uncertainty with another high-resolution measurement performed at GELINA by Olacel *et al.* [25] using γ spectrometry by employing the GAINS spectrometer. Above 4.5 MeV the results, although higher in magnitude, are following the trend of the evaluations, and are in good agreement with the data of Boschung *et al.* [13] and Kinney *et al.* [15].

VIII. THEORETICAL CALCULATIONS

The results of the present work are compared with theoretical reaction calculations performed with the TALYS 1.9 [62,63] and EMPIRE 3.2 codes. The objective of these calculations was to provide a satisfactory theoretical description of the experimental cross sections studied in this work, while also ensuring that the results for the other open reaction channels are aligned with the existing experimental data. The calculations were performed from 100 keV neutron incident energy up to 20 MeV.

The *"TALYS def."* calculation was based on the default parameters provided by the code. These parameters were tuned in order to achieve an optimal agreement between experimental data and theoretical projections. The optical model used is based on the Koning-Delaroche potential [8]. The discrete levels information was taken from the Reference Input Parameter Library (RIPL-3) [64] and for levels with unknown spins, parities or branching rations the code always assigned a value based on statistical rules. For the level density description, instead of the phenomenological model used in the default calculation, a more microscopic approach was used, developed by Goriely on the basis of Hartee-Fock calculations

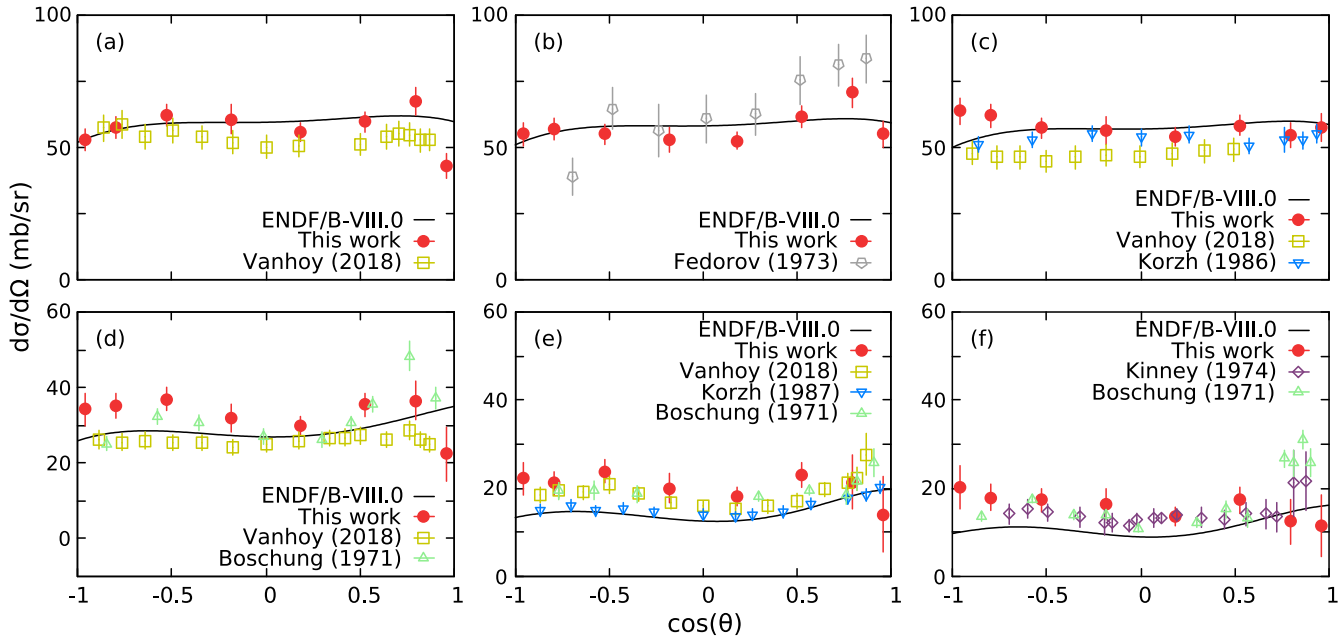

FIG. 13. Comparison of differential cross sections of neutron inelastic scattering from the first excited state of ^{54}Fe as a function of the cosine of the scattering angle θ, with data available in literature and the angular distributions provided in the ENDF/B-VIII.0 evaluation [58]. The t.o.f. intervals that have been selected correspond to neutrons energy ranges (a) $E = 2.750$–2.774 MeV, (b) $E = 2.894$–2.919 MeV, (c) $E = 2.998$–3.023 MeV, (d) $E = 3.973$–4.014 MeV, (e) $E = 4.973$–5.029 MeV, (f) $E = 5.455$–5.521 MeV.

[65,66]. In addition, for the modeling of the γ decay, instead of the phenomenological γ-strength functions model of Kopecky and Uhl [67] used in the default calculation, the microscopic Skyrme-Hartee-Fock-Bogoliubov model was used [68]. The last two changes were made in order to better reproduce the (n, p) and (n, α) reaction cross sections.

In the "*TALYS mic.1-2*" calculations the semi-microscopic spherical optical model potential of Bauge *et al.* [69] was used. For the level density description the most recent microscopic approach based on Hartee-Fock-Bogoliubov calculations using the Gogny force was implemented [70], and for the γ-ray strength functions the microscopic Gogny-Hartee-Fock-Bogoliubov model, developed based on the D1M version of the Gogny force, was used [71]. The difference between the two microscopic calculations *"mic.1"* and *"mic.2"* lies in the normalization

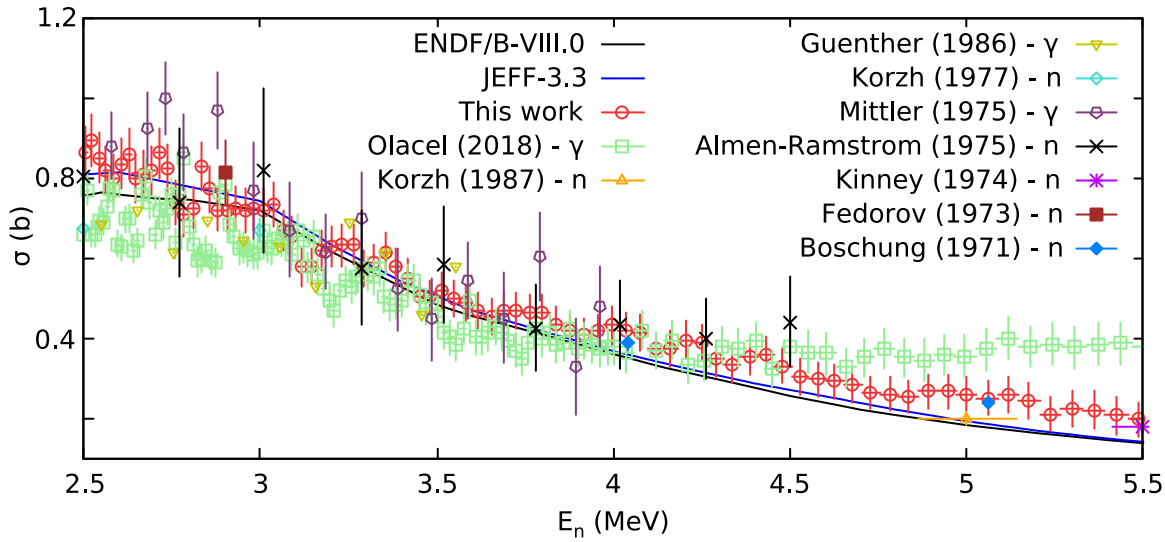

FIG. 14. Angle-integrated cross section of neutron inelastic scattering from the first excited state of ^{54}Fe as a function of the neutron incident energy compared with data available in the EXFOR library [10] and the JEFF-3.3 [4] and ENDF/B-VIII.0 evaluations [58]. The experiments in which the γ-ray emitted from the deexcitation of the first excited state is detected are noted with "-γ" while the ones in which the neutron is detected are noted with "-n".

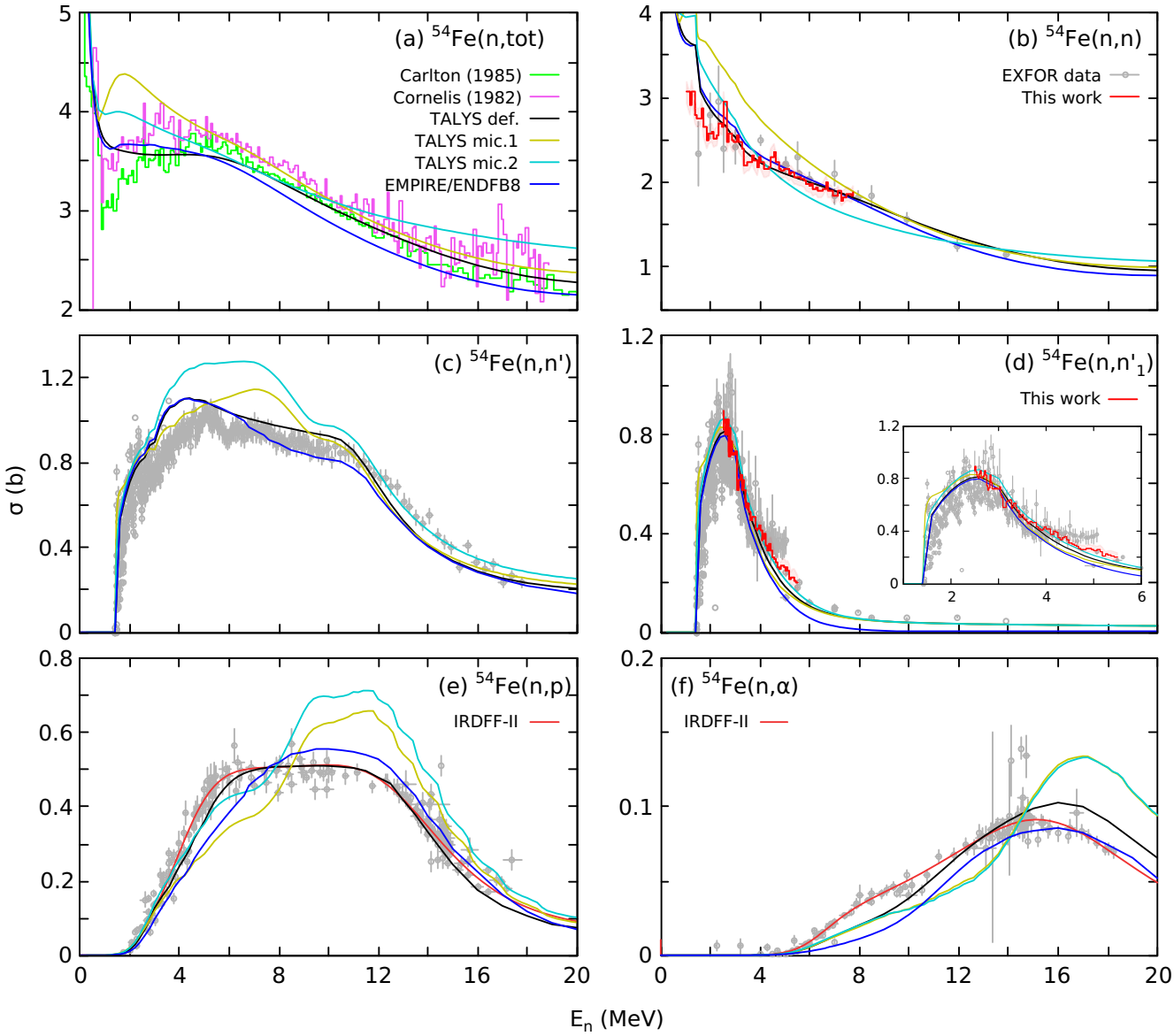

FIG. 15. Comparison between the theoretical calculations of TALYS [62,63] using different sets of parameters (see text below), EMPIRE [60] parametrized based on the ENDF/B-VIII.0 [58] evaluation, and the available experimental data in the literature for the ^{54}Fe total, elastic, inelastic, (n, p), and (n, α) reaction cross sections. The elastic and inelastic scattering data from this work are also included in the graphs. For the ^{54}Fe(n, n'_1) reaction cross section, a subplot is included focused on the neutron energy region studied in this work.

factor used for the imaginary potential of the optical model. In the first case the default value is used, while in the second case an energy dependent factor is used, recommended for energies below 1 MeV.

The *"EMPIRE/ENDFB8"* calculation was based on the parameters reported in the ENDF/B-VIII.0 evaluation for ^{54}Fe. This calculation was triggered by the fact that the elastic scattering cross section of ENDF/B-VIII.0, above 1 MeV neutron energy, was calculated using the EMPIRE code. The optical model potential of Koning-Delaroche was used for neutrons and protons, while for the description of alpha particles the potential of Avrigeanu *et al.* was used [72]. The optical model parameters of the potentials (real/imaginary potential depth, diffuseness, radius), were rescaled according to the values proposed in the evaluation file. For the preequilibrium emission the PCROSS phenomenological model, implemented in the code, was used with a mean free path parameter set to 2.4 [73,74]. To address the correlation between incident and exit channels in elastic scattering the model developed by Hofmann, Richert, Tepel, and Weidenmueller (HRTW) was used for neutron incident energies up to 12.10 MeV [75]. The modified Lorentzian (MLO1) approach was used for the modeling of the γ-ray strength functions [76]. The level density was calculated using the Gilbert-Cameron (GC) model, with some of the αparameters modified according to the evaluation [77].

In Fig. 15 the results of the theoretical calculations are presented for the ^{54}Fe total, elastic, inelastic, (n, p), and (n, α)

reaction cross sections. The calculations are compared with the results of this work and the available experimental data in the literature. For the ^{54}Fe(n, tot) reaction [Fig. 15(a)] the calculations are compared with the high-resolution measurements of Cornelis *et al.* [78] and Carlton *et al.* [61]. To make the comparison easier, the experimental data were averaged over 100 keV energy bins. It is observed that below 4 MeV neutron incident energy the theoretical calculations differ significantly in trend compared to the experimental data over the whole energy region. Above 4 MeV the *"TALYS def."* calculation is able to better reproduce the experimental data, while the *"EMPIRE/ENDFB8"* calculation is systematically lower by 5% over the whole energy region. The microscopic approach "*TALYS mic.1*" is in agreement with the data of Cornelis between 4 and 20 MeV, and the "*TALYS mic.2*" calculation seems to produce higher results above 10 MeV.

In Fig. 15(b) the elastic scattering cross section calculations are compared with the results of this work and the available data in the EXFOR library. It is seen that below 2 MeV the results of both codes suggest higher cross section values than the ones produced in this work. Between 2 and 8 MeV the "*TALYS def.*" and *"EMPIRE/ENDFB8"* calculations are in agreement within uncertainty with the data of this work, while the microscopic calculations seem to perform poorly in this region. Above 8 MeV all calculations are in agreement within uncertainty with the only available experimental data in this region by El-Kadi *et al.* For the inelastic scattering cross sections [total in Fig. 15(c) and partial in Fig. 15(d)] the theoretical predictions follow the same trend as the experimental data. In the total inelastic scattering both codes produce higher cross sections compared to the EXFOR data in the energy range between 3 and 6 MeV, where the cross section reaches maximum values, and from 6 to 12 MeV EMPIRE produces lower cross section than TALYS, but both remain in agreement within the uncertainty of the experimental data. In the case of the partial inelastic scattering from the first excited state of ^{54}Fe, there is an overall good agreement between the theoretical calculations, the results of this work, and the experimental data in literature up to almost 4 MeV neutron incident energy. Above this energy, the TALYS calculations are in good agreement with the data available in literature, while the cross section from EMPIRE falls rapidly.

For the charged particle emitting reactions [(n, p) in Fig. 15(e) and (n, α) in Fig. 15(f)], the calculations are again compared with the data available in the EXFOR library [79–120] and the IRDFF-II evaluation library [121] since the ^{54}Fe(n, p) reaction is a dosimetry standard reaction cross section. For the (n, p) reaction it is observed that the "*TALYS def.*" calculation follows the same trend as the IRDFF-II evaluations and is able to reproduce the "flat" behavior of the cross section between 5 and 12 MeV, whereas *"EMPIRE/ENDFB8"* is in agreement with the EXFOR data only above 12 MeV. In the case of the (n, α) reaction, it seems that both codes perform poorly from the threshold up to 12 MeV, while at higher energies *"EMPIRE/ENDFB8"* is closer to the experimental data. For both reactions, the microscopic predictions of TALYS perform poorly over the whole energy range.

IX. CONCLUSIONS

In this work, a new experiment was performed at GELINA to measure the neutron angular distributions, and cross sections of the ^{54}Fe(n, n) and ^{54}Fe(n, n') reactions in the fast neutron energy range. For the detection of the scattered neutrons the ELISA setup was used, a spectrometer consisting of 32 liquid organic scintillators. The analysis procedure of data obtained with the ELISA spectrometer is briefly described. The process of modeling the response function for each detector individually by combining experimental measurements and Monte Carlo simulation is outlined. The study includes the pulse shape analysis, the treatment of the data for the background contribution by subtracting the sample-out from the sample-in measurement, the elastic/inelastic separation by using kinematic calculations, the multiple scattering correction implementing a Monte Carlo simulation of the whole setup, and the analysis of the fission chamber data to extract the neutron fluence impinged on the ^{54}Fe sample. The differential cross section was then calculated at eight detection angles using Eq. (4) and the integral cross section using the Gauss-Legendre quadrature rule [Eq. (1)]. The whole analysis procedure was successfully validated using the $^{\mathrm{nat}}$C measurement by reproducing the well known $^{\mathrm{nat}}$C(n, n) reaction cross section. The results were compared with the data available in the EXFOR library and the JEFF-3.3 and ENDF-B/VIII.0 evaluations.

For elastic scattering, this is the first experimental measurement providing high-resolution data in the energy range of 1 to 8 MeV. The total uncertainties vary from 5% to 25% for the differential cross section, and from 5% to 8% for the angle integrated cross section. The results are in overall good agreement with the values proposed by the JEFF-3.3 and ENDF/B-VIII.0 evaluations, other experimental data available in the EXFOR library, and the theoretical calculations above 2 MeV incident energy.

The inelastic scattering from the first excited state of ^{54}Fe was also explored and good quality results were extracted in the energy range of 2.5 to 5.5 MeV. In this case, the total uncertainties vary from 7% to 50% for the differential cross section, and from 6% to 20% for the angle integrated cross section. The high uncertainties are observed in the forward detection angles, where the difference between elastic and inelastic scattering cross section is considerable. Also, the calculated differential cross section are slightly higher than the values proposed by ENDF/B-VIII.0, while for the angle integrated results the cross section is in better agreement with the JEFF-3.3 evaluation and the theoretical calculations up to 4 MeV.

The results were also compared with theoretical calculations performed with the TALYS 1.9 and EMPIRE 3.2 nuclear reaction codes. The comparison concluded that the phenomenological approach of the *"TALYS def."*, and *"EMPIRE/ENDFB8"* calculations is in good agreement with the experimental results of this work, and also produce overall better results than those deduced from the microscopic model approach ("*TALYS mic.1-2*").

ACKNOWLEDGMENTS

The authors would like to thank the staff of GELINA for providing the conditions needed for this experiment. This work was partially supported by the Commissariat à l'énergie atomique et aux énergies alternatives (CEA) through the SINET project, and by the European Commission through the EUFRAT [122], and ARIEL (EURATOM research and training program 2014–2018 under Grant Agreement No. 847594) projects [123].

[1] G. Aliberti, G. Palmiotti, M. Salvatores, T. K. Kim, T. Taiwo, M. Anitescu, I. Kodeli, E. Sartori, J. C. Bosq, and J. Tommasi, Nuclear data sensitivity, uncertainty and target accuracy assessment for future nuclear systems, Ann. Nucl. Energy **33**, 700 (2006).

[2] P. Romojaro, F. Álvarez Velarde, O. Cabellos, N. García-Herranz, and A. Jiménez-Carrascosa, On the importance of target accuracy assessments and data assimilation for the co-development of nuclear data and fast reactors: MYRRHA and ESFR, Ann. Nucl. Energy **161**, 108416 (2021).

[3] J. Engelen, H. A. Abderrahim, P. Baeten, D. De Bruyn, and P. Leysen, MYRRHA: Preliminary front-end engineering design, Int. J. Hydrogen Energy **40**, 15137 (2015).

[4] A. Plompen, O. Cabellos, C. De Saint Jean, M. Fleming, A. Algora, M. Angelone, P. Archier, E. Bauge, O. Bersillon, A. Blokhin, F. Cantargi, A. Chebboubi, C. J. Diez, H. Duarte, E. Dupont, J. Dyrda, B. Erasmus, L. Fiorito, U. Fischer, D. Flammini *et al.*, The joint evaluated fission and fusion nuclear data library, JEFF-3.3, Eur. Phys. J. A **56**, 181 (2020).

[5] M. B. Chadwick, E. Dupont, E. Bauge, A. Blokhin, O. Bouland, D. A. Brown, R. Capote, A. Carlson, Y. Danon, C. De Saint Jean, M. Dunn, U. Fischer, R. A. Forrest, S. C. Frankle, T. Fukahori, Z. Ge, S. M. Grimes, G. M. Hale, M. Herman, A. Ignatyuk *et al.*, The CIELO Collaboration: Neutron reactions on ^{1}H, ^{16}O, ^{56}Fe, ^{235,238}U, and ^{239}Pu, Nucl. Data Sheets **118**, 1 (2014).

[6] M. Herman, A. Trkov, R. Capote, G. P. A. Nobre, D. A. Brown, R. Arcilla, Y. Danon, A. Plompen, S. F. Mughabghab, Q. Jing, G. Zhigang, L. Tingjin, L. Hanlin, R. Xichao, L. Leal, B. V. Carlson, T. Kawano, M. Sin, S. P. Simakov, and K. Guber, Evaluation of neutron reactions on iron isotopes for CIELO and ENDF/B-VIII.0, Nucl. Data Sheets **148**, 214 (2018).

[7] INDEN - International Nuclear Data Evaluation Network, https://www-nds.iaea.org/INDEN/ (2017).

[8] A. Koning and J. Delaroche, Local and global nucleon optical models from 1 keV to 200 MeV, Nucl. Phys. A **713**, 231 (2003).

[9] M. Diakaki, S. Chen, G. Noguere, D. Bernard, P. Tamagno, and P. Archier, Evaluation of neutron induced reactions on ^{56}Fe with CONRAD, EPJ Web Conf. **239**, 11005 (2020).

[10] N. Otuka, E. Dupont, V. Semkova, B. Pritychenko, A. I. Blokhin, M. Aikawa, S. Babykina, M. Bossant, G. Chen, S. Dunaeva, R. A. Forrest, T. Fukahori, N. Furutachi, S. Ganesan, Z. Ge, O. O. Gritzay, M. Herman, S. Hlavač, K. Katō, B. Lalremruata *et al.*, Towards a more complete and accurate experimental nuclear reaction data library (EXFOR): international collaboration between nuclear reaction data centres (NRDC), Nucl. Data Sheets **120**, 272 (2014).

[11] Y. Dong and H. Junde, Nuclear data sheets for A = 54, Nucl. Data Sheets **121**, 1 (2014).

[12] W. L. Rodgers, E. F. Shrader, and J. T. Lindow, Neutron scattering from ^{12}C, ^{54}Fe, ^{56}Fe, ^{65}Cu, ^{58}Ni58, and ^{60}Ni, Atomic Energy Commission Progress Report No. 1573-33, Chicago Operations Office, 1967 (unpublished).

[13] P. Boschung, J. T. Lindow, and E. F. Shrader, Scattering of fast neutrons by ^{12}C, ^{54}Fe, ^{56}Fe, ^{58}Ni and ^{60}Ni, Nucl. Phys. A **161**, 593 (1971).

[14] M. B. Fedorov and T. I. Jakovenko, The scattering of 2.9 MeV neutrons by even even isotopes of iron, chromium and zinc, Ukr. Fiz. Zh. **19**, 152 (1974).

[15] W. E. Kinney and F. G. Perey, ^{54}Fe neutron elastic and inelastic scattering cross sections from 5.50 to 8.50 MeV, Oak Ridge National Laboratory Technical Report, 1974 (unpublished).

[16] I. A. Korzh, V. A. Mishchenko, E. N. Mozhzhukhin, N. M. Pravdivyy, and I. E. Sanzhur, Differential neutron scattering cross-sections at 1.5 to 3.0 MeV for titanium, iron and bismuth nuclei, Ukr. Fiz. Zh. **22**, 87 (1977).

[17] S. M. El-Kadi, C. E. Nelson, F. O. Purser, R. L. Walter, A. Beyerle, C. R. Gould, and L. W. Seagondollar, Elastic and inelastic scattering of neutrons from ^{54,56}Fe and ^{63,65}Cu: (I). Measurements from 8 to 14 MeV and a spherical optical model analysis, Nucl. Phys. A **390**, 509 (1982).

[18] I. A. Korzh, V. A. Mishchenko, and N. M. Pravdivyi, Fast neutron elastic and inelastic scattering cross sections of ^{54}Fe, Sov. At. Energy **62**, 487 (1987).

[19] P. T. Guenther, D. L. Smith, A. B. Smith, and J. F. Whalen, Total, scattering and gamma-ray-production cross sections for few-MeV neutrons on ^{54}Fe, Ann. Nucl. Energy **13**, 601 (1986).

[20] J. R. Vanhoy, S. H. Liu, S. F. Hicks, B. M. Combs, B. P. Crider, A. J. French, E. A. Garza, T. Harrison, S. L. Henderson, T. J. Howard, M. T. McEllistrem, S. Nigam, R. L. Pecha, E. E. Peters, F. M. Prados-Estévez, A. P. D. Ramirez, B. G. Rice, T. J. Ross, Z. C. Santonil, L. C. Sidwell, J. L. Steves, B. K. Thompson, and S. W. Yates, ^{54}Fe neutron elastic and inelastic scattering differential cross sections from 2–6 MeV, Nucl. Phys. A **972**, 107 (2018).

[21] D. Ene, C. Borcea, S. Kopecky, W. Mondelaers, A. Negret, and A. Plompen, Global characterisation of the GELINA facility for high-resolution neutron time-of-flight measurements by Monte Carlo simulations, Nucl. Instrum. Methods Phys. Res., Sect. A **618**, 54 (2010).

[22] K. Tsukada, S. Tanaka, Y. Tomita, and M. Maruyama, Elastic and inelastic scattering of fast neutrons from iron, nickel and tungsten, Nucl. Phys. A **125**, 641 (1969).

[23] E. Ramström, A systematic study of neutron inelastic scattering in the energy range from 2.0 MeV to 4.5 MeV, Aktiebolaget Atomenergi, Stockholm/Studsvik Report No. 503, 1975 (unpublished).

[24] A. Mittler, J. Nardini, and G. P. Couchell, Measurements of neutron inelastic scattering cross sections for natural iron, data from CSISRS file, 1975.

[25] A. Olacel, C. Borcea, M. Boromiza, P. Dessagne, G. Henning, M. Kerveno, L. Leal, A. Negret, M. Nyman, and A. J. M. Plompen, Neutron inelastic scattering on ^{54}Fe, Eur. Phys. J. A **54**, 183 (2018).

[26] E. Pirovano, R. Beyer, M. Dietz, A. R. Junghans, S. E. Müller, R. Nolte, M. Nyman, A. J. M. Plompen, M. Röder, T. Szücs, and M. P. Takacs, Cross section and neutron angular distribution measurements of neutron scattering on natural iron, Phys. Rev. C **99**, 024601 (2019).

[27] E. Pirovano, R. Beyer, A. Junghans, R. Nolte, M. Nyman, and A. Plompen, Measurements of neutron scattering angular distributions with a new scintillator setup, EPJ Web Conf. **146**, 11008 (2017).

[28] M. Nyman, T. Adam, C. Borcea, M. Boromiza, P. Dessagne, G. Henning, M. Kerveno, A. Negret, A. Olacel, E. Pirovano *et al.*, New equipment for neutron scattering cross-section measurements at GELINA, EPJ Web Conf. **239**, 17003 (2020).

[29] Eljen Technology, EJ301, EJ309 data sheet available at https://eljentechnology.com/products/liquid-scintillators/ej-301-ej-309.

[30] Eljen Technology, EJ315 data sheet available at, 2023.

[31] E. Pirovano, Neutron scattering cross section measurements with a new scintillator array, Ph.D. thesis, Ghent University, 2017 (unpublished).

[32] D. Gedcke and W. McDonald, A constant fraction of pulse height trigger for optimum time resolution, Nucl. Instrum. Methods **55**, 377 (1967).

[33] L. Bardelli, G. Poggi, M. Bini, G. Pasquali, and N. Taccetti, Time measurements by means of digital sampling techniques: A study case of 100 ps FWHM time resolution with a 100MSample/s, 12bit digitizer, Nucl. Instrum. Methods Phys. Res., Sect. A **521**, 480 (2004).

[34] M. A. Nelson, B. D. Rooney, D. R. Dinwiddie, and G. S. Brunson, Analysis of digital timing methods with BaF2 scintillators, Nucl. Instrum. Methods Phys. Res., Sect. A **505**, 324 (2003), Special Issue, Proceedings of the tenth Symposium on Radiation Measurements and Applications.

[35] I. Pawełczak, S. Ouedraogo, A. Glenn, R. Wurtz, and L. Nakae, Studies of neutron–γ pulse shape discrimination in EJ-309 liquid scintillator using charge integration method, Nucl. Instrum. Methods Phys. Res., Sect. A **711**, 21 (2013).

[36] F. Brooks, A scintillation counter with neutron and gamma-ray discriminators, Nucl. Instrum. Methods **4**, 151 (1959).

[37] J. Polack, M. Flaska, A. Enqvist, C. Sosa, C. Lawrence, and S. Pozzi, An algorithm for charge-integration, pulse-shape discrimination and estimation of neutron/photon misclassification in organic scintillators, Nucl. Instrum. Methods Phys. Res., Sect. A **795**, 253 (2015).

[38] A. Tomanin, J. Paepen, P. Schillebeeckx, R. Wynants, R. Nolte, and A. Lavietes, Characterization of a cubic EJ-309 liquid scintillator detector, Nucl. Instrum. Methods Phys. Res., Sect. A **756**, 45 (2014).

[39] H. Klein and S. Neumann, Neutron and photon spectrometry with liquid scintillation detectors in mixed fields, Nucl. Instrum. Methods Phys. Res., Sect. A **476**, 132 (2002), Special Issue, International Workshop on Neutron Field Spectrometry in Science, Technology and Radiation Protection.

[40] N. Kornilov, I. Fabry, S. Oberstedt, and F.-J. Hambsch, Total characterization of neutron detectors with a ^{252}Cf source and a new light output determination, Nucl. Instrum. Methods Phys. Res., Sect. A **599**, 226 (2009).

[41] H. Klein, Neutron spectrometry in mixed fields: NE213/BC501A liquid scintillation spectrometers, Radiat. Prot. Dosim. **107**, 95 (2003).

[42] C. J. Werner, J. Bull, C. Solomon, F. Brown, G. McKinney, M. Rising, D. Dixon, R. Martz, H. Hughes, L. Cox *et al.*, MCNP6.2 release notes, Los Alamos National Laboratory Report No. LA-UR-18-20808, 2018 (unpublished).

[43] C. J. Werner *et al.*, MCNP users manual–code version 6.2, Los Alamos National Laboratory Report No. LA-UR-17-29981, 2017 (unpublished).

[44] C. Rouki, P. Archier, C. Borcea, C. De Saint Jean, J. Drohé, S. Kopecky, A. Moens, N. Nankov, A. Negret, G. Noguère, A. Plompen, and M. Stanoiu, High resolution measurement of neutron inelastic scattering cross-sections for ^{23}Na, Nucl. Instrum. Methods Phys. Res., Sect. A **672**, 82 (2012).

[45] C. Budtz-Jørgensen, H. Knitter, and G. Bortels, Assaying of targets for nuclear measurements with a gridded ionization chamber, Nucl. Instrum. Methods Phys. Res., Sect. A **236**, 630 (1985).

[46] A. Ramirez, E. Peters, J. Vanhoy, S. Hicks, L. Alasagas, D. Alcorn-Dominguez, S. Block, S. Byrd, E. Chouinard, B. Combs, B. Crider, E. Derdyn, L. Downes, J. Erlanson, S. Evans, A. French, E. Garza, J. Girgis, T. Harrison, S. Henderson *et al.*, Neutron elastic and inelastic scattering differential cross sections on carbon, Nucl. Phys. A **1023**, 122446 (2022).

[47] A. Smith, R. Holt, and J. Whalen, Neutron interaction with carbon-12 in the few-MeV region, Nucl. Sci. Eng. **70**, 281 (1979).

[48] H. Knox, J. Cox, R. Finlay, and R. Lane, Differential cross section and polarization for 2.63 MeV neutrons scattered from ^{12}C, Nucl. Phys. A **217**, 611 (1973).

[49] R. O. Lane, R. D. Koshel, and J. E. Monahan, Polarization and differential cross section for neutrons scattered from ^{12}C, Phys. Rev. **188**, 1618 (1969).

[50] A. Langsdorf, R. O. Lane, and J. E. Monahan, Angular distributions of scattered neutrons, Phys. Rev. **107**, 1077 (1957).

[51] H. B. Willard, J. K. Bair, and J. D. Kington, Elastic scattering angular distributions of fast neutrons on light nuclei, Phys. Rev. **98**, 669 (1955).

[52] M. Walt and J. R. Beyster, Interaction of 4.1-Mev neutrons with nuclei, Phys. Rev. **98**, 677 (1955).

[53] M. R. MacPhail, Anomalous scattering of fast neutrons, Phys. Rev. **57**, 669 (1940).

[54] E. Haddad and D. D. Phillips, Elastic and inelastic scattering of neutrons from ^{12}C, Bull. Am. Phys. Soc. Ser. II **4**, 358(J2) (1959).

[55] N. Bostrom, I. Morgan, J. Prud'homme, P. Okhuysen, and O. Hudson, Neutron interactions in lithium, carbon, nitrogen, aluminum, argon, manganese, yttrium, zirconium, radiolead and bismuth, Wright Air Development Center Report No. 59, 1959 (unpublished).

[56] F. Perey and W. Kinney, Carbon neutron elastic-and inelastic-scattering cross sections from 4.5 to 8.5 MeV, Oak Ridge National Laboratory Report No. 4441, 1969 (unpublished).

[57] F. Perey and W. Kinney, Elastic and inelastic scattering cross sections in the energy range 5.2–8.7 MeV, U.S. AEC Nuclear Cross Sections Advisory Committee Report No. 42, 1978 (unpublished), p. 190.

[58] D. Brown, M. Chadwick, R. Capote, A. Kahler, A. Trkov, M. Herman, A. Sonzogni, Y. Danon, A. Carlson, M. Dunn, D. Smith, G. Hale, G. Arbanas, R. Arcilla, C. Bates, B. Beck, B. Becker, F. Brown, R. Casperson, J. Conlin *et al.*, ENDF/B-VIII.0: The 8th major release of the nuclear reaction

data library with CIELO-project cross sections, new standards and thermal scattering data, Nucl. Data Sheets **148**, 1 (2018), Special Issue on Nuclear Reaction Data.

[59] A. Carlson, V. Pronyaev, R. Capote, G. Hale, Z.-P. Chen, I. Duran, F.-J. Hambsch, S. Kunieda, W. Mannhart, B. Marcinkevicius, R. Nelson, D. Neudecker, G. Noguere, M. Paris, S. Simakov, P. Schillebeeckx, D. Smith, X. Tao, A. Trkov, A. Wallner, and W. Wang, Evaluation of the neutron data standards, Nucl. Data Sheets **148**, 143 (2018).

[60] M. Herman, R. Capote, B. Carlson, P. Obložinský, M. Sin, A. Trkov, H. Wienke, and V. Zerkin, EMPIRE: Nuclear reaction model code system for data evaluation, Nucl. Data Sheets **108**, 2655 (2007).

[61] R. Carlton, J. Harvey, and B. Castel, Single particle strength in ^{55}Fe, Bull. Am. Phys. Soc. Ser. II **30**, 1252 (1985).

[62] A. J. Konning, S. Hilaire, and M. C. Duijvestijn, *TALYS-1.0* (EDP Sciences, Les Ulis, France, 2008), p. 211.

[63] TALYS 1.9, available at https://www-nds.iaea.org/talys/, 2023.

[64] R. Capote, M. Herman, P. Obložinský, P. Young, S. Goriely, T. Belgya, A. Ignatyuk, A. Koning, S. Hilaire, V. Plujko, M. Avrigeanu, O. Bersillon, M. Chadwick, T. Fukahori, Z. Ge, Y. Han, S. Kailas, J. Kopecky, V. Maslov, G. Reffo, M. Sin, E. Soukhovitskii, and P. Talou, RIPL – reference input parameter library for calculation of nuclear reactions and nuclear data evaluations, Nucl. Data Sheets **110**, 3107 (2009), Special Issue on Nuclear Reaction Data.

[65] S. Goriely, S. Hilaire, and A. J. Koning, Improved microscopic nuclear level densities within the Hartree-Fock-Bogoliubov plus combinatorial method, Phys. Rev. C **78**, 064307 (2008).

[66] S. Goriely, F. Tondeur, and J. Pearson, A Hartree–Fock nuclear mass table, At. Data Nucl. Data Tables **77**, 311 (2001).

[67] J. Kopecky and M. Uhl, Test of gamma-ray strength functions in nuclear reaction model calculations, Phys. Rev. C **41**, 1941 (1990).

[68] S. Goriely, E. Khan, and M. Samyn, Microscopic HFB + QRPA predictions of dipole strength for astrophysics applications, Nucl. Phys. A **739**, 331 (2004).

[69] E. Bauge, J. P. Delaroche, and M. Girod, Lane-consistent, semimicroscopic nucleon-nucleus optical model, Phys. Rev. C **63**, 024607 (2001).

[70] S. Hilaire, M. Girod, S. Goriely, and A. J. Koning, Temperature-dependent combinatorial level densities with the D1M Gogny force, Phys. Rev. C **86**, 064317 (2012).

[71] S. Goriely, S. Hilaire, S. Péru, and K. Sieja, Gogny-HFB+QRPA dipole strength function and its application to radiative nucleon capture cross section, Phys. Rev. C **98**, 014327 (2018).

[72] V. Avrigeanu, P. E. Hodgson, and M. Avrigeanu, Global optical potentials for emitted alpha particles, Phys. Rev. C **49**, 2136 (1994).

[73] J. J. Griffin, Statistical model of intermediate structure, Phys. Rev. Lett. **17**, 478 (1966).

[74] C. Cline, The Pauli exclusion principle in pre-equilibrium decay, Nucl. Phys. A **195**, 353 (1972).

[75] H. Hofmann, J. Richert, J. Tepel, and H. Weidenmüller, Direct reactions and Hauser-Feshbach theory, Ann. Phys. **90**, 403 (1975).

[76] V. Plujko, A new closed-form thermodynamic approach for radiative strength functions, Acta Phys. Pol. B **31**, 435 (2000).

[77] A. Gilbert and A. G. W. Cameron, A composite nuclear-level density formula with shell corrections, Can. J. Phys. **43**, 1446 (1972).

[78] E. Cornelis, L. Mewissen, and F. Poortmans, Neutron resonance structure of Fe-54 and Fe-56 from high resolution total cross section measurements, in *Conf. on Nucl. Data for Sci. and Technol., Antwerp, Belgium* (1982), p. 135.

[79] A. Filatenkov, Neutron activation cross sections measured at KRI in neutron energy region 13.4–14.9 MeV, USSR Report to the I.N.D.C. No. 0460, 2016 (unpublished).

[80] W. Mannhart and D. Schmidt, Measurement of neutron activation cross sections in the energy range from 8 MeV to 15 MeV, Phys. Techn. Bundesanst., Neutronenphysik Report No. 53, 2007 (unpublished).

[81] T. Shimizu, H. Sakane, M. Shibata, K. Kawade, and T. Nishitani, Measurements of activation cross sections of (n,p) and (n,a) reactions with d-D neutrons in the energy range of 2.1–3.1 MeV, Ann. Nucl. Energy **31**, 975 (2004).

[82] J. Meadows, D. Smith, L. Greenwood, R. Haight, Y. Ikeda, and C. Konno, Measurement of fast-neutron activation cross sections for copper, europium, hafnium, iron, nickel, silver, terbium and titanium at 10.0 and 14.7 MeV and for the Be(d,n) thick-target spectrum, Ann. Nucl. Energy **23**, 877 (1996).

[83] A. Grallert, J. Csikai, C. Buczko, and I. Shaddad, Investigations on the systematics in (n,a) cross sections at 14.6 MeV, IAEA Nucl. Data Section Report to the I.N.D.C. No. 286, 1993 (unpulbished), p. 131.

[84] I. Garlea, C. Miron-Garlea, H. Rosu, G. Fodor, and V. Raducu, Integral neutron cross sections measured around 14 MeV, Rev. Roum. Phys. **37**, 19 (1992).

[85] S. K. Saraf, C. E. Brient, P. M. Egun, S. M. Grimes, V. Mishra, and R. S. Pedroni, Cross sections and spectra for the ^{54}Fe and ^{56}Fe (n,xp) and (n,xa) reactions between 8 and 15 MeV, Nucl. Sci. Eng. **107**, 365 (1991).

[86] J. W. Meadows, D. L. Smith, L. R. Greenwood, L. P. Geraldo, W. Mannhart, G. Boerker, and G. Mueller, Measurements of the neutron cross section for ^{54}Fe$(n,\alpha)^{51}$Cr between 5.3 and 14.6 MeV, in *Conf. on Nucl. Data for Sci. and Technol., Juelich, Germany* (1991), p. 288.

[87] A. Ercan, M. N. Erduran, M. Subasi, E. Gueltekin, G. Tarcan, A. Baykal, and M. Bostan, 14.6 MeV neutron induced reaction cross section measurements, in *Conf. on Nucl. Data for Sci. and Technol., Juelich, Germany* (1991), p. 376.

[88] G. P. M. Viennot, M. Berrada, and S. Joly, Cross-section measurements of (n,p) and (n,np + pn + d) reactions for some titanium, chromium, iron, cobalt, nickel, and zinc isotopes around 14 MeV, Nucl. Sci. Eng. **108**, 289 (1991).

[89] I. Kimura and K. Kobayashi, Calibrated fission and fusion neutron fields at the Kyoto University reactor, Nucl. Sci. Eng. **106**, 332 (1990).

[90] Y. Ikeda, C. Konno, K. Kosako, and K. Oishi, Activation cross section measurement at a neutron energy range from 2.1 to 3.0 MeV by d-d neutron source at FNS, Japanese Report to NEANDC No. 155, 1990 (unpublished), p. 11.

[91] L. R. Greenwood, Recent research in neutron dosimetry and damage analysis for materials irradiations, American Society of Testing and Materials Report No. 956, 1987 (unpublished), p. 743.

[92] B. M. Bahal and R. Pepelnik, Cross section measurements of Cr, Mn, Fe, Co, Ni for an accurate determination of these elements in natural and synthetic samples using a 14 MeV

neutron generator, Ges.Kernen.-Verwertung, Schiffbau and Schiffahrt, No.85-E-11 (1985).
[93] Fan Peiguo, Zhao Wenrong, Teng Dan, and Lu Hanlin, Measurements of cross sections for some reactions induced by 8.62 MeV neutrons, Chin. J. Nucl. Phys. **7**, 242 (1985).
[94] I. Garlea, C. Miron-Garlea, H.N. Rosu, M. Ion, and V. Raducu, Neutron cross sections measured at 14.8 MeV, Zentralinst. f. Kernforschung Rossendorf Report No. 562, 1985 (unpublished), p. 126.
[95] O. I. Artem'ev, I. V. Kazachevskii, V. N. Levkovskii, V. L. Poznyak, and V. F. Reutov, Cross sections for (n,p) and (n,alpha) reactions on chromium, iron, copper, and molybdenum nuclei at a neutron energy of 14.8 MeV, Sov. At. Energy **49**, 655 (1980).
[96] A. Paulsen, R. Widera, F. Arnotte, and H. Liskien, Cross sections for the reactions ^{54}Fe(n,a)^{51}Cr, ^{54}Fe(n,p)^{54}Mn, and ^{56}Fe(n,p)^{56}Mn, Nucl. Sci. Eng. **72**, 113 (1979).
[97] K. Fukuda, K. Matsuo, S. Shirahama, and I. Kumabe, Activation cross sections on Fe, Co, Ni, Zr and Mo for 14.6 MeV neutrons, Japanese Report to NEANDC No. 56, 1978 (unpublished), p. 44.
[98] C.-F. Ai, M.-W. Wu, and J.-C. Chou, Measurements of Al-27(n,p)Mg-27 and Fe-54(n,p)Mn-54 cross sections, Nucl. Sci. **14**, 1 (1977).
[99] D. L. Smith and J. W. Meadows, Cross-section measurement of (n,p) reactions for ^{27}Al, ^{46,47,48}Ti, ^{54,56}Fe, ^{58}Ni, ^{59}Co, and ^{64}Zn from near threshold to 10 MeV, Nucl. Sci. Eng. **58**, 314 (1975).
[100] J. J. Singh, Neutron reaction cross sections of iron at 14.5 MeV, Trans. Am. Nucl. Soc. **15**, 147 (1972).
[101] A. Paulsen and R. Widera, Ni-58(N,P)Co-58 and Fe-54(N,P)Mn-54 cross-section measurements for use as threshold detectors, in *Chemical Nucl. Data Conf., Canterbury, UK* (1971), p. 129.
[102] S. M. Qaim, R. Woelfle, and G. Stoecklin, Activation cross sections of fast neutron induced nuclear reactions: precision measurements and systematics, in *Chemical Nucl. Data Conf., Canterbury, UK* (1971), p. 121.
[103] R. C. Barrall, J. A. Holmes, and M. Silbergeld, High energy neutron cross section validation and neutron flux spectrum using the HENRE source, Air Force Special Weapons Center Kirtland A.F.B. Report No. 68, 1969 (unpublished), p. 134.
[104] R. C. Barrall, M. Silbergeld, and D. G. Gardner, Cross sections of some reactions of Al, S, Mn, Fe, Ni, In and I with 14.8 MeV neutrons, Nucl. Phys. A **138**, 387 (1969).
[105] P. V. Rao and R. W. Fink, Neutron reaction cross sections of selenium and iron at 14.4 MeV, Phys. Rev. **154**, 1023 (1967).
[106] E. E. Carroll and G. G. Smith, Iron-54(n,p) cross-section measurement, Nucl. Sci. Eng. **22**, 411 (1965).
[107] S. R. Salisbury and R. A. Chalmers, ^{54}Fe(n,p), (n,a), (n,2n) cross sections, Phys. Rev. **140**, B305 (1965).
[108] A. Lauber and S. G. Malmskog, Measurements of the ^{54}Fe(n,p)^{54}Mn reaction cross section in the neutron energy range 2.3–3.8 MeV, Nucl. Phys. **73**, 234 (1965).
[109] W. G. Cross and H. L. Pai, Activation cross sections in Ti for 14.5 MeV neutrons, Canadian Report to EANDC No. 16, 1963 (unpublished), p. 1.
[110] H. Pollehn and H. Neuert, Bestimmung von Wirkungsquerschnitten einiger Kernreaktionen durch 14 MeV-Neutronen nach einer Aktivierungsmethode, Z. Naturforsch. A **16**, 227 (1961).
[111] J. Van Loef, Activation cross sections for (n,p) reactions in some medium-weight nuclei with D+D neutrons, Nucl. Phys. **24**, 340 (1961).
[112] D. Allan, The energy and angular distribution of protons from 14 MeV neutron reactions with Fe54, Nucl. Phys. **10**, 348 (1959).
[113] H. Bai, H. Jiang, Y. Lu, Z. Cui, J. Chen, G. Zhang, Y. M. Gledenov, M. V. Sedysheva, G. Khuukhenkhuu, X. Ruan, H. Huang, J. Ren, and Q. Fan, ^{56,54}Fe$(n,\alpha)^{53,51}$Cr cross sections in the MeV region, Phys. Rev. C **99**, 024619 (2019).
[114] T. Khromyleva, I. Bondarenko, A. Gurbich, V. Ketlerov, V. Khryachkov, and P. Prusachenko, Investigation of (n,a) reaction cross sections for a number of structural material isotopes, Nucl. Sci. Eng. **191**, 282 (2018).
[115] Z. Wang, X. Fan, L. Zhang, H. Bai, J. Chen, G. Zhang, Yu. M. Gledenov, M. V. Sedysheva, L. Krupa, and G. Khuukhenkhuu, Cross sections of the ^{56}Fe$(n,\alpha)^{53}$Cr and ^{54}Fe$(n,\alpha)^{51}$Cr reactions in the MeV region, Phys. Rev. C **92**, 044601 (2015).
[116] Yu. M. Gledenov, M. V. Sedysheva, G. Khuukhenkhuu, S. Bao, G. Tang, Z. Chen, and Y. Chen, Study of the fast neutron induced (n,a) reaction for middle-mass nuclei, in *Conf. on Nucl. Data for Sci. and Techn., Trieste, Italy* (1997), Vol. 1, p. 514.
[117] N. I. Molla and S. M. Qaim, A systematic study of (n,p) reactions at 14.7 MeV, Nucl. Phys. A **283**, 269 (1977).
[118] G. N. Maslov, F. Nasyrov, and N. F. Pashkin, Experimental cross-sections for nuclear reactions involving neutrons with energies of about 14 MeV, USSR Report to the I.N.D.C. No. 42, 1974 (unpublished), p. 10.
[119] Y. Ikeda, C. Konno, K. Oishi, T. Nakamura, H. Miyade, K. Kawade, H. Yamamoto, and T. Katoh, Activation cross section measurements for fusion reactor structural materials at neutron energy from 13.3 to 15.0 MeV using FNS facility, JAERI Repor No. 1312, 1988 (unpublished).
[120] L. Hanlin, L. Jizhou, F. Peiguo, and H. Jianzhou, Measurements of cross sections of reactions (n,p) and (n,a) for ^{54}Fe, ^{181}Ta, Chin. J. Nucl. Phys. **4**, 272 (1982).
[121] A. Trkov, P. Griffin, S. Simakov, L. Greenwood, K. Zolotarev, R. Capote, D. Aldama, V. Chechev, C. Destouches, A. Kahler, C. Konno, M. Koštál, M. Majerle, E. Malambu, M. Ohta, V. Pronyaev, V. Radulović, S. Sato, M. Schulc, E. Šimečková, I. Vavtar, J. Wagemans, M. White, and H. Yashima, IRDFF-II: A new neutron metrology library, Nucl. Data Sheets **163**, 1 (2020).
[122] S. Oberstedt, G. Sibbens, S. Kopecky *et al.*, EUFRAT, Open Access to the nuclear research infrastructure at JRC Geel – Summary report 2017–2018 (European Commission, Joint Research Centre, Publications Office, 2018), https://data.europa.eu/doi/10.2760/798329.
[123] C. Franzen, A. R. Junghans, E. M. Gonzalez, and A. J. M. Plompen, ARIEL & SANDA nuclear data activities, EPJ Nuclear Sci. Technol. **8**, 19 (2022).